Assessing the combined effects of local climate and mounting configuration on the electrical and thermal performance of photovoltaic systems. Application to the greater Sydney area

Alessia Boccalatte, Martin Thebault, Riccardo Paolini, Marco Fossa, Julien Ramousse, Christophe Ménézo, Mattheos Santamouris

Assessing the Combined Effects of Local Climate and Mounting Configuration on the Electrical and Thermal Performance of Photovoltaic Systems. Application to the Greater Sydney Area

Alessia Boccalatte[a,c], Martin Thebault[a], Riccardo Paolini[b], Marco Fossa[c], Julien Ramousse[a], Christophe Ménézo[a], Mattheos Santamouris[b]

[a] LOCIE, Université Savoie Mont Blanc, CNRS, UMR5271, F-73376 Le Bourget du Lac, France
[b] Faculty of Built Environment, University of New South Wales (UNSW), Sydney, NSW2052, Australia
[c] DIME - Department of Mechanical, Energy, Management and Transportation Engineering, University of Genova, Italy

[*]Corresponding author e-mail: alessia.boccalatte@unige.it

Abstract

Extremely high urban temperatures adversely affect photovoltaic (PV) system performance. Accurate PV cell temperature assessment relies on local weather conditions, exacerbated by urban overheating, often overlooked by inadequate temperature models and non-local data. This study investigates the electrical and thermal PV performance, considering mounting configurations and local conditions. Data from ten weather stations in Greater Sydney (NSW) during 2016-2017, including a hot summer, are used. The Sandia model is used to predict cell temperatures and power output for four mounting configurations, from open rack to building-integrated (BIPV). A PV thermal model is implemented to analyse daytime convection, crucial for understanding PV impact on local climate. Results show peak cell temperatures of 60°C (open rack) to over 90°C (BIPV), causing up to 50% power loss and 11% reduction in monthly performance ratio. Local climate variations impact PV energy output up to 6%, with mounting configuration effects up to 11%. Daytime convective flux averages 150-180 W/m², peaking at 700 W/m². Convective release varies up to 22% based on local climate, generally higher for open rack than close roof mounts, with potential reversals under low wind speed conditions. These findings can improve the knowledge of PV performances in urban areas facing extreme temperatures.

Keywords: Urban Overheating, Photovoltaic (PV) system performance, Mounting configurations, Daytime convective flux

1. Introduction

The impact of climate change on air temperature trends and the rise of heatwaves in cities warrants careful attention. Urban overheating, a significant research topic worldwide, results in higher temperatures in cities compared to surrounding rural areas [1–4]. Unlike regional heatwaves, urban overheating is a local phenomenon influenced by complex factors, including urban morphology [5–7], prevailing weather conditions [8], and the extreme weather events [9,10].
In various regions, including Australia, high air temperatures in urban areas adversely affect PV system performance [11], with projections indicating potential unprecedented temperatures of 50°C in major Australian cities under a 2°C global warming scenario [12]. Comparative studies show that Australia experiences higher PV degradation rates, ranging from -1.35% to -1.46% per year, compared to the UK's rate of -1.05% to -1.16% per year [13]. A previous investigation conducted by EnergyAustralia [14]

examined the performance of rooftop PV systems installed for the Sydney Olympic Games in 2000 and found that nearly 20% of the analysed systems underperformed.
The PV market has experienced substantial growth in grid-connected photovoltaic systems, with significant integration on rooftops. In 2021, the Australian market saw a surge in solar installations, with 4.9 GW of new capacity, of which over 3 GW consisted of rooftop PV systems. Residential roofs accounted for 1.7 GW, while commercial and industrial roofs contributed 1.3 GW [15,16].
Despite the annual mean daily solar irradiation in Australia ranges from 16 MJ/m^2 day in southern regions to 22 MJ/m^2 day in northern areas [17], PV system performance and reliability are significantly impacted by high air temperatures and extreme climatic conditions [18,19], raising concerns about long-term efficiency [11,20].
In light of this global scenario, comprehensive analyses are critical to realistically predict PV system performance and optimize their deployment in urban areas, where heat mitigation strategies are vital. Urban overheating is an escalating worldwide concern, necessitating attention and appropriate strategies for adequate PV development in urban settings.

1.1 Insights from previous research on Urban Overheating in Sydney

Previous research on urban overheating has highlighted the significance of this phenomenon as a global concern. In coastal cities like Sydney, intricate interactions between synoptic climatology and local factors can impact overheating dynamics [21]. Sydney's geographical location along the eastern coastline of the South Pacific Ocean exposes the city to coastal and desert winds, presenting challenges in understanding urban heat islands (UHI) resulting from coastal-inland airflows [22,23].
Previous research by Santamouris et al. [24] analysed a 10-year climatic dataset from six meteorological stations in the Greater Sydney, revealing significant variations in UHI intensity ranging from 0 to 11°C. These variations arise from the interaction between the cooling mechanism of sea breezes and the heating mechanism of westerly winds, leading to a pronounced divergence in the UHI effect between eastern and western parts of the city. Despite higher tree canopy cover and lower built density, western areas of Sydney exhibit stronger UHI effects due to reduced influence from sea breezes. Yun et al. [22] investigated urban overheating in Sydney using hourly temperature measurements collected over an 18-year period from eight different sites within a 50 km radius from the coastline. They found that Urban Heat Island Intensity (UHII) was negative during the night and evening hours and positive during the central hours of the day (between 10 am and 4 pm), peaking around 3 pm. The highest UHII values occurred during summer (November to February), with peak values ranging from 3.7°C to 8.5°C, proportional to the distance from the coast. Khan et al. [25] examined the interaction between urban overheating and heatwave periods in the Greater Sydney region, finding that the average peak difference between the urban overheating magnitude during heatwave periods and non-heatwave periods was 8°C in western Sydney, and 4-4.5°C in inner Sydney.
Regarding the effects of urban overheating in Sydney, Vaneckova at al. reported a 4.5-12% increase in mortality rate in Sydney, due to a 10°C rise in daily maximum temperatures and high concentrations of ozone and particulate matter [26]. Previous studies also investigated the impact of overheating on building cooling demand, finding that western Sydney suburbs have considerably higher Cooling Degree Days (approximately three times higher than those observed in the eastern part), thus leading an increase of cooling demand [27].

1.2 Research gap and aim of the study

Previous literature has explored urban overheating dynamics in Greater Sydney, emphasizing its negative effects on building energy consumption [27] and mortality [26]. However, despite the substantial increase of roof-mounted PV systems, no prior study related to the Sydney metropolitan area has specifically addressed the impact of local climate patterns on their performance. Existing findings related to Sydney indicate that urban overheating peaks during the central hours and summer,

exacerbated by the increasing frequency of heatwaves. Of particular concern are the future projections that indicate a significant temperature rise, especially in the newly developed western and southwestern urban areas [28], particularly vulnerable to overheating due to desert winds' heating mechanism. Given these factors, and considering the ongoing urban expansion into these areas, comprehending the impact of local overheating phenomena on PV systems is crucial.

The primary objective of this study is to investigate the thermal and electrical performance of PV systems, assessing the influence of Sydney urban overheating and mounting configurations, with a specific focus on periods of exceptionally high temperatures during the summer periods. It is worth noting that while previous literature has extensively explored PV system performance under various working conditions at the national [11,29–33] or regional scale [34–36], the present research takes a more in-depth approach by considering local climate patterns at the metropolitan scale which have not been previously addressed. This site-specific approach may be relevant in densely populated metropolitan areas like Sydney, where overheating patterns are particularly various and pronounced.

To achieve the aim of the study, one year of experimental weather data from ten local weather stations in the Greater Sydney region (2016-2017) is utilized. The study employs the detailed Sandia Array Performance Model (SAPM) to uncover significant differences in mounting configurations, often overlooked in conventional models. Additionally, a PV thermal model is developed to analyse daytime heat fluxes. This aspect is crucial for urban PV installations, as simulations have shown that integrating PV systems on building roofs may increase local air temperatures by 0.6-2.3°C in Sydney during summer [37].

The conclusions drawn from this study hold relevance beyond the Greater Sydney region, emphasizing the importance of incorporating local climate data and mounting configurations into the planning of PV systems to address the pertinent factors influencing their performance. Furthermore, this research underscores the necessity of implementing solutions for mitigating PV temperature rise, as explored and proposed in various previous studies within the literature [38–40].

The subsequent sections outline key aspects of PV performance models and the indirect impact of PV systems on the urban microclimate, providing the necessary background for framing the research and its objectives.

1.3 PV temperature models and effect of local climate conditions on PV performance

The performance of PV modules is greatly affected by cell temperatures, which directly determine energy output and heat dissipation. Cell efficiency is typically rated under Standard Test Conditions (STC) at 25°C cell temperature, 1,000 W/m^2 irradiance, and air mass of 1.5. Nevertheless, real-world outdoor installations experience non-STC conditions, resulting in varying cell temperatures influenced by local weather [29,41–46]. Operating temperatures often exceed 25°C, leading to reduced efficiency compared to the rated value. The temperature coefficient for crystalline silicon cells indicates approximately 0.4% efficiency reduction per 1°C increase above the STC reference temperature, resulting in up to 30% lower power production compared to STC conditions [47]. Furthermore, PV overheating can cause delamination, hot spots, and damage adhesive seals [48,49].

Accurate PV cell temperature prediction is crucial for evaluating installation efficiency and converting module performance from standard rating temperature (25°C) to actual operating temperatures. In absence of direct measurements, PV models are used to estimate cell temperature. Many proposed models for PV cell temperature prediction have been extensively validated against experimental data. Skoplaki and Playvos [50] reviewed approximately 40 correlations, implicit and explicit, for calculating operating temperatures. These correlations involve environmental variables and numerical parameters, which are material and/or system dependent. Therefore, careful selection of a suitable expression considering specific climate conditions, mounting configuration, and integration level with the building is necessary.

Correlations commonly used in the field estimate cell temperature by utilizing the Nominal Operating Cell Temperature (NOCT). The NOCT represents the average temperature of a PV module in open rack installations under Standard Operating Conditions (irradiance: 800 W/m^2, ambient temperature: 20°C, tilt angle: 45°, wind speed: 1 m/s, open circuit operation). However, several studies evidence the sensitivity of PV temperature predictions to wind speed conditions [33,51]. Using correlations based on NOCT, wind speed is not accounted for, and the method is limited to open rack applications leading to an underestimation of PV cell operating temperatures by up to 20°C in integrated systems [52].
To address the limitations of the NOCT model, various empirical and semi-empirical models have been proposed, including the Sandia PV Array Performance Model (SAPM) by King et al. [53], the Faiman model [54], the model proposed by Muzathik [55], the Skoplaki model [56], the Fuentes model [57], the Ross model [58]. The SAPM has shown better performance compared to the abovementioned models under different climatic conditions [59,60], notably when wind speed exceeds 6 m/s, and under hot desert climate conditions [61].
The Sandia model is used for the present analyses as it offers greater flexibility than the other models as it allows considering three different mounting setups (open rack, close roof mount, and insulated back) and two module types (glass/cell/glass and glass/cell/polymer sheet). The influence of mounting configuration on PV cell temperatures has been deeply analysed since, as shown in several studies, it represents a critical parameter for PV performance assessment [33,62,63].

1.4 Indirect effects of PVs on urban climate

PV modules, having lower thermal inertia than other surfaces, quickly heat up and release absorbed solar energy through radiation and convection [64]. The convective heat flux between modules and surrounding air is crucial, influenced by factors such as temperature difference, local wind speed, and PV mounting configuration. Experimental studies show that when PV modules are exposed to hot climate conditions like Arizona (US) and Libya (Africa), the PV cell temperatures can reach up to 90°C and 125°C, respectively [65–67]. Beyond the reduced efficiency and power generation, the thermal effects of urban PV installations may have implications for the overall urban energy balance [37,64].
Previous studies on urban PV system impacts on air temperatures have yielded conflicting results, often due to errors and inappropriate assumptions [47,64,68–72]. Common limitations of existing approaches include the use of the "effective albedo" and the neglect of convective heat released by the back PV surface in rooftop applications [73]. To understand the indirect effects on the microclimate, empirical studies and accurate modelling of convective and radiative heat transfer are crucial. Recent literature studies have shown advancements in this area by including the modelling of the surfaces shaded by PV modules [68,69,74,75]. Tools like UCR-Solar$_{roof}$ have been recently developed to accurately represent the sensible heat transfers of rooftop PV installations [70].
This study further develops a PV thermal model to explore daytime heat released through convection and radiation. Note that it does not assess PV systems' impact on the urban microclimate, which would require more complex modelling. The focus remains on quantifying electrical performance and understanding the influence of climatic conditions and mounting configurations on daytime heat fluxes.

2. Materials and methods

Section 2 is devoted to describing the data and models employed in this analysis. It is organized as follows: Section 2.1 provides an overview of the meteorological data obtained from ten selected weather stations in the Greater Sydney region. In Section 2.2, the primary geomorphological characteristics and local climate influences of the study area are presented, highlighting the distinctions between the western and eastern suburbs. Section 2.3 outlines the Sandia Array Performance model (SAPM), which is employed to conduct precise calculations on various selected figures of merit, further explained in Section 2.4. Lastly, Section 2.5 details the developed thermal PV model, specifically designed for calculating the daytime sensible heat based on the PV mounting configuration.

2.1 Measured data from local weather stations

The objective of this study is to evaluate the performance of photovoltaic systems installed in various locations within the Greater Sydney, located in New South Wales, Australia. The Greater Sydney area encompasses the city of Sydney and its surroundings, including the local government areas of Sydney, Parramatta, Blacktown, Penrith, Liverpool, Campbelltown, and Sutherland. The region covers an approximate land area of 12,368 km^2, extending from the coastline in the east to the Blue Mountains in the west, spanning about 70 km. The climate in the region is classified as a humid subtropical climate (Köppen Geiger climate classification, type Cfa).
Hourly meteorological data from ten different weather stations have been utilized in this research. These data were collected by the Australian Bureau of Meteorology (BoM) between May 2016 and April 2017 [76]. The Greater Sydney region and the geographical distribution of the selected weather stations is illustrated in Figure 1. The different colours attributed to each weather station refers to the territorial partitioning which is further detailed in the following Section 2.2.

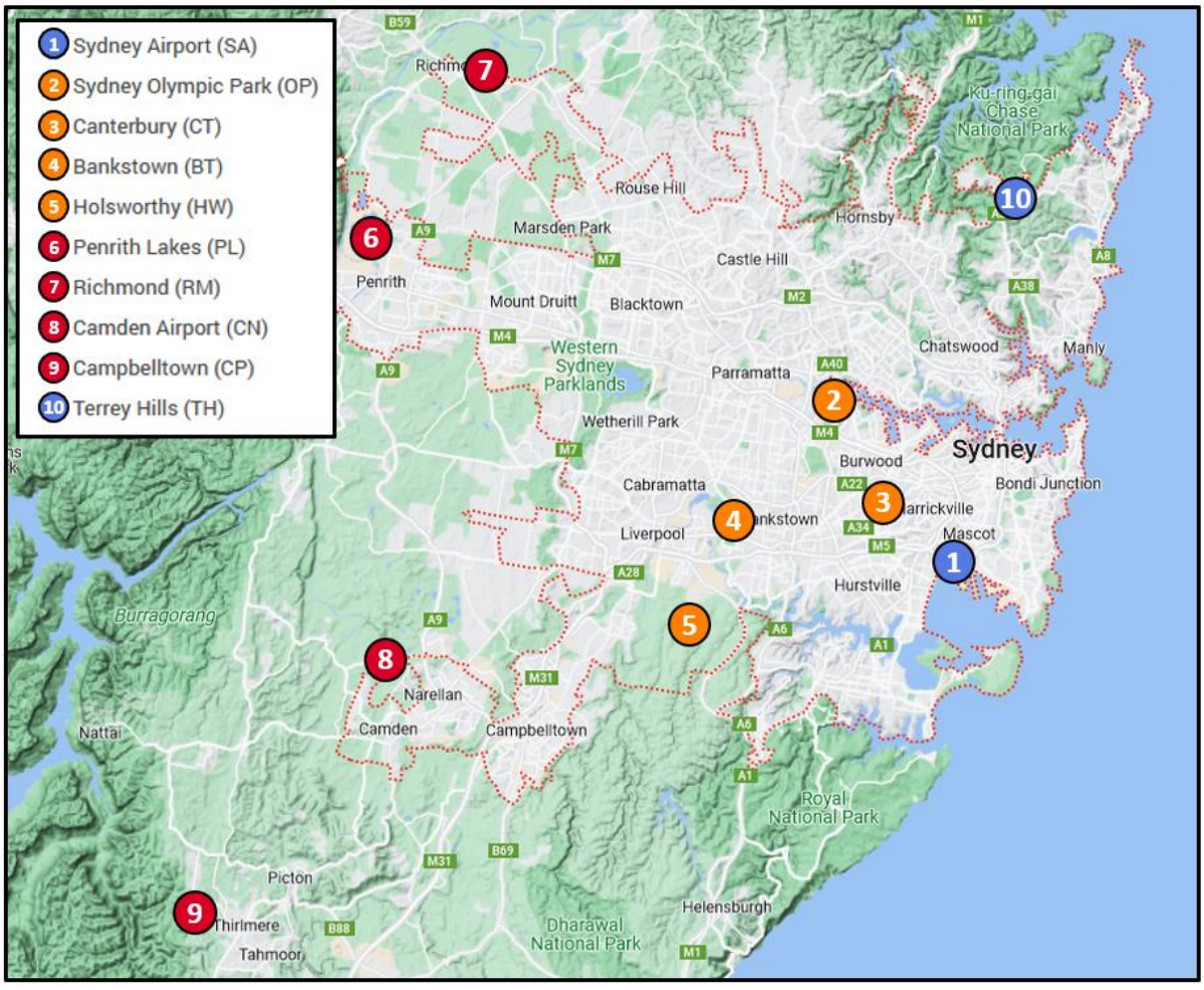

Figure 1: Analysed weather stations across the greater Sydney region

The station ID assigned by the Bureau of meteorology (BoM), the geographical coordinates, and the elevation of the selected weather stations are presented in Table 1.

Table 1: Description of the selected weather stations.

Weather Station	Station ID	Latitude (°S)	Longitude (°E)	Elevation (m)
Sydney Airport AMO (SA)	66037	-33.9465	151.1731	6.0
Sydney Olympic Park AWS (OP)	66212	-33.8338	151.0718	4.0
Canterbury Racecourse AWS (CT)	66194	-33.9057	151.1134	3.0
Bankstown Airport AWS (BT)	66137	-33.9181	150.9864	6.5
Holsworthy Aerodrome AWS (HW)	66161	-33.9925	150.9489	68.2
Penrith Lakes AWS (PL)	67113	-33.7195	150.6783	24.7
Richmond RAAF (RM)	67105	-33.6004	150.7761	19.0
Camden Airport AWS (CN)	68192	-34.0157	150.6910	73.9
Campbelltown – Mount Annan (CP)	68257	-34.0615	150.7735	112.0
Terrey Hills AWS (TH)	66059	-33.6908	151.2253	199.0

The measured meteorological variables include dry bulb and wet bulb air temperature, which have been used to compute relative humidity, as well as wind speed and direction, air pressure, and daily cumulative rainfall from 9 am. Global horizontal solar radiation data have been sourced from Macquarie University (latitude: -33.7748, longitude: 151.1111, elevation: 66.8 m) due to the unavailability of equally precise information for the analysed weather station. It has been assumed to be uniform across all weather stations owing to the low spatial variability of irradiance intensity within the study area [77]. While pivotal for territorial-scale analyses, at the metropolitan scale, a prior study in Sydney [78] indicated that the variation in irradiance intensity among four weather stations in the Greater Sydney area can be considered negligible, falling below 1%. Consequently, this parameter is regarded to exert minimal influence on the outcomes. The Reindl et al. [79] model is used to derive diffuse radiation whereas the variant of the Prata model proposed by Lindberg et al. [80] is used for infrared radiation. To ensure data quality, all raw data underwent filtering, validation, and gap filling using artificial intelligence techniques, as fully detailed in Yun et al. [22].

2.2 Study area and territorial partitioning

Based on the latest census of the Australian Bureau of Statistics, the Greater Sydney region had a total population of 5.2 million people in 2021, with a total site area of 12,368 km^2 [81]. This translates to a population density of approximately 428 persons per square kilometer. The region is surrounded by several national parks to the north and south, and the estimated total built area is approximately 4,196 km^2. In the last years, urban expansion has predominantely occurred in western suburbs, which are projected to accommodate more than 50% of the population of the Greater Sydney region by 2036 [28]. For the purposes of this study, the Greater Sydney area is subdivided into three zones: eastern (coastal), inner, and western areas, based on their proximity to the coastline, as previously shown through different colours in Figure 1.

The Sydney Airport (SA) weather station in eastern Sydney is located on the coast in proximity to Botany Bay and it is surrounded by Sydney inner suburbs on its non coastal boundaries. The land surrounding Sydney Airport is a mixed-use development with aviation purposes, and residential, commercial, and industrial areas.

Inner Sydney comprises of Olympic Park (OP), Canterbury (CT), Bankstown (BT), and Holsworthy (HW). The distance of the inner suburbs from the nearest coast ranges from 7 km (CT) to about 16 km

(BT and HW). Sydney Olympic Park, located approximately 14 km west of the Sydney Central Business District (CBD), is in close proximity to significant water features such as the Parramatta River, wetlands, and scattered waterways. The surrounding areas are predominantly sparsely built mixed-use areas with some commercial, recreational, and parkland land uses. Canterbury and Bankstown are inner suburbs characterized by open, low-rise mixed-use and residential buildings, with high built and population density in Canterbury. Holsworthy Aerodrome is situated far from the Sydney CBD, near the district of Liverpool, within a densely vegetated area.

Western Sydney includes the Penrith Lakes (PL), Richmond (RM), Camden Airport (CN), and Campbelltown (CP) weather stations. These stations are the farthest from both the CBD and the coastline and are generally characterized by low-density built areas, multiple bodies of water, wetlands, and extensive tree canopy. Camden Airport (CN) and Campbelltown (CP) are more peripheral compared to Penrith Lakes (PL) and Richmond (RM), with Campbelltown (CP) weather station being slightly outside the administrative boundaries of Greater Sydney.

Terrey Hills (TH) weather station deviates slightly from the defined territorial partitioning as it is located in the northern forest district at an elevation of 199 m above sea level. It is positioned 25 km north of Sydney CBD and 7.5 km from the nearest coastline, encompassing a large area of dense greenery, including national parks, bushland, and reserves, with a total tree canopy cover of approximately 58%.

The tree canopy cover is higher for the Western Sydney sites (25-35%), compared to inner and eastern Sydney where it is around 15-17% [82]. The distance from the nearest coast increases in Western Sydney, with Penrith Lakes situated 50 km away, while other Western Sydney sites are approximately 30 km from the nearest coast. Inner Sydney sites are located 8-12 km from the coast, and the Sydney CBD is situated near the coastline.

In this study, the local climate conditions of the ten weather stations are analyzed, focusing on yearly summary statistics of air temperature and wind speed values. Additionally, the impact of local climate conditions on electricity demand for cooling purposes is assessed through the calculation of Cooling Degree Hours (CDH). CDH is calculated as the sum of positive hourly differences between outdoor air temperature and a base temperature, which in this case is set at 19.5°C based on the Australian Energy Market Operator (AEMO) guidelines for New South Wales [83]. The formula for calculating CDH is described in Eq. 1

$$CDH = \sum_{i=1}^{N} \left(T_{air} - T_{ref}\right) \qquad for\ T_{air} > T_{ref} \tag{1}$$

Here, N is the number of hours over a selected time period (day, month, year), T_{air} is the hourly air temperature, and T_{ref} is the reference base temperature.

2.3 The Sandia Array Performance Model (SAPM)

Several photovoltaic (PV) performance models have been developed and documented in the literature to assess the power production of PV systems [84]. These models vary in complexity, with some based on generalized system assumptions, while others incorporate manufacturer parameters, derived quantities, and empirically derived data. For this study, the Sandia Array Performance Model (SAPM) developed by the US Sandia National Laboratories (SNL) has been chosen due to its proven accuracy in relation to field measurements [53].

The SAPM is an empirically formulated model that employs a steady-state approach and relies on empirically derived module parameters obtained from day-long I-V measurements conducted on modules from various manufacturers. Through testing PV modules under non-standard conditions, the SAPM accounts for the influences of cell temperature, spectral variations, and angle of incidence, enabling the linearization of most elements in the form of a five-equation model. For a comprehensive understanding of the model and equations, the interested reader is referred to the original source [53] for a detailed description, which is omitted here for brevity.

The SAPM model has recently been integrated into the pvlib Python library [85], which is used to calculate PV power output. The primary inputs for the model include the plane of array solar irradiance incident on the module surface, as well as wind speed and ambient air temperature, which are required for estimating the PV cell temperature through the Sandia thermal model.
In this analysis, the focus is on c-Si modules, specifically the Canadian Solar 300 Watt Solar Module, which is assumed to be inclined at a tilt angle of 28 degrees and oriented towards the north. This tilt angle is chosen to be close to both the optimal angle for maximizing yearly energy yield and the typical slope of roofs in the Sydney area [87]. The technical specifications of the Canadian Solar 300 Watt Solar Module are summarized in Table 2.

Table 2: PV module technical specifications

Name	Canadian Solar 300 Watt Solar Module
Model	CS6X-300M
Manufacturer	Canadian Solar
Year	2013
Material	Monocrystalline Silicon
Cells in series	72
STC Power Rating	300 W
Peak Efficiency	15.63%
I_{mpo}	8.22 A
V_{mpo}	36.5 V
I_{sco}	8.74 A
V_{oco}	45 V
Temp. Coefficient of Power	-0.45%/K

The SAPM operating PV cell temperature (T_c) is defined through Eq. 2

$$T_c = T_m + \left(\frac{G_{POA}}{G_{STC}}\right) \cdot \Delta T \tag{2}$$

Where G_{POA} is the plane of array (POA) irradiance incident on module surface [W/m^2], G_{STC} is the irradiance at Standard Test Conditions (STC), namely 1000 W/m^2, ΔT is the temperature difference [°C] between the PV cell and the back surface of the module at G_{STC} irradiance level, and T_m is the back-surface module temperature [°C] which can be calculated based on Eq. 3

$$T_m = G_{POA} \cdot \{e^{a+b \cdot WS}\} + T_a \tag{3}$$

Where WS is the wind speed [m/s], T_a is the ambient air temperature [°C], and a and b are empirically determined coefficients depending on the module type and the mounting configuration. ΔT, a, and b can be derived from Table 3 [53].

Table 3: Modelling parameters based on module type and mounting configuration

Module type	**Mount**	**a**	**b**	**ΔT (°C)**
Glass/cell/glass	Open rack	-3.47	-0.0594	3
Glass/cell/glass	Close roof mount	-2.98	-0.0471	1
Glass/cell/polymer sheet	Open rack	-3.56	-0.0750	3
Glass/cell/polymer sheet	Insulated back	-2.81	-0.0455	0

The configurations include "Glass/Cell/Glass" module type with an open rack or close roof mount, as well as "Glass/Cell/Polymer Sheet" module type with an open rack or insulated back. These configurations represent different scenarios with varying degrees of air flow and heat transfer behind the PV modules, ranging from maximum air flow (open rack) to limited air flow (close roof mount) to insulated back surfaces representing building-integrated applications (BIPV). These four configurations, along with local air temperature and wind speed data from ten selected weather stations, are utilized to compute the PV cell temperatures and power production.

2.4 Figures of merit of PV performance assessment

Based on the previous section discussing the calculation of PV power production using the SAPM model, various figures of merit are selected to analyse the impact of local climate, PV configuration, and high temperature conditions on the electrical performance of PV installations. These figures of merit include efficiency, normalized efficiency, temperature losses, performance ratio, and photovoltaic production, which provide valuable insights into the performance of the PV system.

The PV module efficiency (η_{PV}) quantifies the electrical efficiency of the PV module. It is calculated as the ratio of the DC power generated by the PV array system to the plane of array irradiance received by the module as in Eq. 4

$$\eta_{PV}(t) = \frac{P(t)}{G_{POA}(t)} \tag{4}$$

where P is the DC power generated by the PV array system per unit surface [W/m^2] and G_{POA} is the plane of array (POA) irradiance received by the module per unit surface [W/m^2].

The normalized efficiency (η_N) is another important parameter that considers the rated PV power at Standard Test Conditions and normalizes the DC power and irradiance based on their respective values at STC. It provides a useful metric that facilitates performance comparisons under different operating conditions and it can be calculated as in Eq. 5

$$\eta_N(t) = \frac{P(t) \cdot \frac{1}{P_{STC}}}{G_{POA}(t) \cdot \frac{1}{G_{STC}}} \tag{5}$$

where P_{STC} is the rated PV power at Standard Test Conditions (STC) of G_{STC}=1000 W/m^2, T_c=25°C, and air mass of 1.5.

To quantify the impact of high temperatures on PV production, the power losses due to temperature ($P^*_{loss,T}$) are evaluated. This metric compares the actual DC power generated by the PV array system at a given temperature to the theoretical DC power at STC cell temperature (T_c=25°C). The power losses due to temperature represent the percentage reduction in power output caused by higher cell temperatures than the reference one and it is defined as in Eq. 6

$$P^*_{loss,T} = \frac{P(t) - P_{25}(t)}{P(t)} \cdot 100\% \tag{6}$$

where P_{25} is the theoretical DC power of the PV array system [W/m^2] at STC cell temperature, namely T_c=25°C.

The Performance Ratio (PR) is an important parameter defined in the IEC 61724 standard for assessing the overall performance of a PV system [88]. The PR represents the ratio of the actual electricity generated by the PV system to the electricity that would have been generated if the system consistently converted sunlight to electricity at the level expected from its DC nameplate rating [89]. The PR can be calculated over a specific time interval τ (typically a day) as the ratio between the Final Yield $Y_{f,\tau}$ and the Reference Yield $Y_{r,\tau}$ as in Eq. 7

$$PR_\tau = \frac{Y_{f,\tau}}{Y_{r,\tau}} = \frac{\frac{1}{P_{STC}} \cdot \sum_\tau P(t) \cdot \Delta t}{\frac{1}{G_{STC}} \sum_\tau G_{POA}(t) \cdot \Delta t} \quad (7)$$

where P_{STC} is the rated PV power at Standard Test Conditions (STC) of G_{STC}=1000 W/m^2, T_c=25°C, and air mass of 1.5, $P_{mp}(t)$ is the DC power generated by the PV array system [W/m^2] and $G_{POA}(t)$ is the plane of array (POA) irradiance received by the module [W/m^2] at time t, and Δt represents the time step.

2.5 Daytime Convective and Radiative Heat Fluxes

In this section, the impact of PV configuration and local climate conditions on the daytime convective and radiative heat fluxes is analysed by introducing the developed thermal PV model.

The Sandia model is effective in predicting the temperatures of photovoltaic (PV) cells during daytime conditions. However, night time temperature predictions are not provided. In this study, the convective and radiative heat fluxes are calculated exclusively during daytime operation when the PV temperature is always higher than the ambient air temperature. Only two out of the three previously considered mounting configurations are analysed: open rack glass/polymer, which exhibits lower temperatures, and close roof mount glass/glass. Insulated back glass/polymer configuration is not considered since their thermal modelling depends on the thermal properties of the roof, whose modelling is beyond the scope of this study. Here, the calculation of the released heat fluxes is exclusively related to the PV module and does not consider the combined effect of PV and the roof. Therefore, the impact of PV on the urban microclimate is not intended to be assessed, as that would require more accurate models and precise information about the roof structure and configuration [69,75]. Instead, the objective is to compare the influence of local climate factors and PV mounting configuration on urban heat transfers.

During daytime operation, the conversion of incident shortwave radiation on the PV module results in the generation of both electrical and thermal energies. Some of this radiation is dissipated as thermal losses through longwave radiation and convection, while the remaining energy is converted into electrical power.

The steady-state heat balance over the PV cell layer (disregarding thermal capacitance) is determined through Eq. 8 [90]:

$$G_{POA}(1 - \rho) - Q_{elec} - Q_{rad} - Q_{conv} - Q_{cond} = 0 \quad (8)$$

here, G_{POA} represents the incident is the plane of array (POA) irradiance on module surface, ρ is the reflectivity of the front glass which is assumed equal to 0.1, Q_{elec} is the energy flux extracted as electrical power, and the remaining terms account for heat losses through radiation (Q_{rad}), convection (Q_{conv}), and conduction (Q_{cond}), all in W/m². Conduction is neglected due to the small contact area between the PV module frame and mounting structure.

The convection model used in this study is based on the DOE-2 algorithm [91], which considers natural and forced convection, as well as surface orientation. The key input parameters for the convection model are wind speed, surface tilt angle, surface temperature, ambient temperature, and roughness coefficients. The convective heat flux [W/m^2] is calculated through Eq. 9

$$Q_{conv} = h_c \cdot (T_{surface} - T_{ambient}) \quad (9)$$

where $T_{surface}$ represents the temperature of the PV front/back surfaces, and $T_{ambient}$ is the temperature of the air in contact with them. Distinctions are made to account for different physical conditions and mounting configurations. For the open rack mounting, the back surface temperature (T_{back}) can be calculated using the equation for the calculation of T_m (Eq. 3) according to the Sandia thermal model. The front surface temperature (T_{front}) is assumed to be equal to the Sandia PV cell temperature T_c (Eq. 2), which ranges from 0 to 3°C higher than the back surface temperature depending on the irradiance levels and mounting configuration. As for $T_{ambient}$, it is assumed to be equal to the air temperature on

both PV sides for the open rack configuration. For the back PV side of the close roof mount configuration, $T_{ambient}$ represents the temperature of the air in the gap between the PV module and the roof and thus it is calculated as the film temperature (T_{film}), which is the average of T_{back} and T_{air}, as in Eq. 10

$$T_{film} = \frac{T_{back} + T_{air}}{2} \tag{10}$$

The convective heat transfer coefficient h_c, according to the DOE-2 convection model [91], is a combination of the natural convection coefficient (h_n) and the forced convection coefficient over a smooth surface ($h_{c,glass}$). The equations used to calculate h_c are Eq. 11 and 12

$$h_c = h_n + R_f \cdot (h_{c,glass} - h_n) \tag{11}$$

$$h_{c,glass} = \sqrt{h_n^2 + (a \cdot [WS]^b)^2} \tag{12}$$

the constants a and b depend on the surface position with respect to the wind direction, where a=3.26 and b=0.89 for windward surfaces, and a=3.55 and b=0.617 for leeward surfaces. A simplifying assumption that the front PV surface is windward, and the bottom is leeward is used based on [75]. R_f represents the surface roughness coefficient, which is assumed to be equal to 1 (very smooth), and WS is the wind speed.

For the close roof mount configuration, the same theoretical model proposed for the open rack PV system applies to the front PV side, considering both natural and forced convection. However, for the back PV side, only natural convection is considered [92,93]. The natural convection component for an upward-facing surface (front PV side) is given by Eq. 13

$$h_n = \frac{9.842 \cdot |\Delta T|^{1/3}}{7.283 - |\cos(\beta)|} \tag{13}$$

and for a downward facing surface (back PV side) is given by Eq. 14

$$h_n = \frac{1.810 \cdot |\Delta T|^{1/3}}{1.382 + |\cos(\beta)|} \tag{14}$$

in these equations, β represents the PV surface tilt angle, and ΔT is the temperature difference between the PV surface and the air temperature.

A summary of the assumptions made for the front and back PV surfaces, as well as the two different mounting configurations, is provided in Table 4.

Table 4: Assumptions for the calculation of the convective heat flux as a function of the PV side and mounting configuration

	$T_{surface}$ (Eq. 9)	$T_{ambient}$ (Eq. 9)	h_c (Eq. 11)	a, b (Eq. 12)
Open rack (front PV side)	T_c (Eq. 2)	T_{air}	DOE-2 algorithm (natural + forced)	Windward (a= 3.26, b=0.89)
Open rack (back PV side)	T_m(Eq. 3)	T_{air}	DOE-2 algorithm (natural + forced)	Leeward (a= 3.55, b=0.617)

Close roof (front PV side)	T_c (Eq. 2)	T_{air}	DOE-2 algorithm (natural + forced)	Windward (a= 3.26, b=0.89)
Close roof (back PV side)	T_m(Eq. 3)	T_{film} (Eq. 10)	DOE-2 algorithm (only natural)	Leeward (a= 3.55, b=0.617)

Concerning the radiation heat transfer rate, it could be theoretically calculated for both the front and back surfaces of the PV module as the summation of the long-wave radiation emitted to the sky (Q_{rad_sky}) and to the ground (Q_{rad_ground}), with some modifications for the close roof mount whose back surface is facing only the roof. The expressions for these components are Eq. 15 to 17

$$Q_{rad,f} = Q_{rad\_sky} + Q_{rad\_ground} \tag{15}$$

$$Q_{rad\_sky} = \mathrm{F}_{pv\_sky} \cdot \varepsilon_{pv} \cdot \sigma \cdot (T_{pv}^4 - T_{sky}^4) \tag{16}$$

$$Q_{rad\_ground} = \mathrm{F}_{pv\_ground} \cdot \varepsilon_{pv} \cdot \sigma \cdot (T_{pv}^4 - T_{ground}^4) \tag{17}$$

where ε_{pv} is the front/back emissivity, F_{pv_sky} and F_{pv_ground} are the view factors of the front/back PV surface with the sky and the ground respectively, T_{pv} is the front/back surface temperature of the PV module, T_{sky} is the effective sky temperature, T_{ground} is the ground temperature (assumed to be equal to T_{air}), and σ is the Stefan-Boltzmann constant.

The effective sky temperature T_{sky} is a straightforward indirect way to calculate the net radiative exchange with the atmosphere. There are many correlations in the literature with air temperature, humidity, time of day, and/or other parameters to estimate sky temperature [94,95]. The most commonly used one is given by Eq. 18 [96]

$$\mathrm{T}_{sky} = 0.0552 \cdot T_{air}^{1.5} \tag{18}$$

However, this correlation applies to clear night time conditions [97] and also the other correlations in the literature are specifically for cloud-free conditions. As recently highlighted by [90] when this correlation is applied to PV temperature models such as in Fuentes model [57] daytime PV temperatures can fall below ambient in particular when irradiance is low.

Based on the above considerations, the radiation heat transfer rate is derived after calculating the convective one based on the PV heat balance equation (Eq. 8).

3. Results and Discussion

The present section (Section 3) outlines and discuss the results obtained through the present research. The section is subdivided as follows: Section 3.1 provides an analysis of the different local climate conditions at the ten considered weather stations, with a particular focus on air temperature, wind speed, and Cooling Degree Hours (CDH). Section 3.2 is dedicated to the analysis of PV operating cell temperatures and performance metrics across the weather station and mounting configurations (Section 3.2.1). It further focuses on the impact of high temperatures on a series of selected figures of merit (Section 3.2.2), on temperature-induced power losses (Section 3.2.3), and on PV production (Section 3.2.4). Finally, the results related to daytime convective and radiative heat fluxes are presented in Section 3.3.

3.1 Local climate conditions across the weather stations

Table 5 provides summary statistics, including mean, standard deviation, minimum, and maximum values, of the measured air temperature and wind speed for each of the ten weather stations during the analyzed period (from May 2016 to April 2017). The weather stations are identified by abbreviations: SA (Sydney Airport), OP (Olympic Park), CT (Canterbury), BT (Bankstown), HW (Holsworthy), PL

(Penrith Lakes), RM (Richmond), CN (Camden Airport), CP (Campbelltown), and TH (Terrey Hills). The table also includes the distance from the nearest coastline (including Sydney Harbour and Botany Bay) and the distance from Sydney Central Business District (CBD), which are measured using GIS tools.

Table 5: Summary statistics of air temperature and wind speed values for each weather station

Weather station										
	SA	OP	CT	BT	HW	PL	RM	CN	CP	TH
Distance from the nearest coast [km]										
	0.1	12.9	6.9	16.3	16.5	47.3	34.5	35.0	39.2	5.6
Distance from Sydney CBD [km]										
	8.7	13.2	9.5	21.0	27.4	51.8	50.1	50.3	72.0	20.1
Air Temperature [°C]										
mean	19.2	18.5	18.1	18.4	17.6	18.5	18.1	17.3	17.1	17.5
std	5.2	6.2	6.0	6.4	6.4	6.8	7.2	7.0	6.8	5.4
min	5.7	2.3	1.2	1.4	0.1	1.5	-1.4	-1.7	-0.4	3.0
max	40.8	43.5	42.9	43.8	44.1	46.4	46.0	44.9	44.7	39.6
Wind speed [m/s]										
mean	5.7	2.4	3.1	3.3	3.2	2.2	2.8	2.5	2.1	2.8
std	2.7	1.8	2.2	2.3	1.8	1.7	2.2	2.2	1.5	1.2
min	0.0	0.0	0.0	0.0	0.0	0.0	0.0	0.0	0.0	0.0
max	16.0	10.0	11.1	12.1	11.8	11.0	12.1	11.7	8.2	11.2

The mean air temperature varies among the weather stations, ranging from 17.1°C to 19.2°C. Station SA, located on the coast in eastern Sydney, records the highest mean temperature of 19.2°C, while station CP, in the western area, has the lowest mean temperature of 17.1°C. This suggests that the proximity to dense urban areas around SA may contribute to higher mean temperatures in that area due to urban overheating. On the other hand, stations CP and CN, which are more peripheral and farther from both the CBD and the coast, experience a mean air temperature that is about 2°C lower. Worth noticing also that CP and CN weather stations, together with TH, have the highest elevation above sea level (Table 1), which can contribute to a faster release of absorbed heat. Focusing on the inner suburbs, HW exhibits lower mean air temperature values compared to other inner stations (OP, CT, BT), potentially influenced by the surrounding densely vegetated areas.

The standard deviation values of air temperature range from 5.2°C to 7.2°C, indicating varying degrees of temperature variability across the stations. Station RM exhibits the highest standard deviation, implying greater temperature fluctuations. This could be attributed to the distance from the coast, as western stations farther from the coast generally experience greater temperature variations (around 6.8°C) compared to eastern/coastal stations such as SA and TH, where the standard deviation of air temperatures is lower (around 5.3°C). Moreover, as observed in prior research [22], Richmond (RM) features extensive woodlands and a scattered built environment, enabling unimpeded flow of the prevailing north-eastern wind and resulting in diminished heat entrapment mechanisms, thereby leading to the noticeable variability.

Analyzing the minimum air temperatures, station CN reports the lowest minimum temperature of -1.7°C, whereas SA and TH, which are nearest to the coast, reach a minimum temperature of about 5.3°C. This observation suggests that coastal locations benefit from the moderating influence of the nearby ocean. Regarding maximum temperatures, the trend appears to be the opposite, with areas farthest from the coast exhibiting higher maximum temperatures. For instance, station PL, located in inner western Sydney, records the highest maximum temperature of 46.4°C. In contrast, stations closer

to the coast, such as TH, do not exceed 39.6°C, and station SA reaches a maximum temperature of 40.8°C.

The mean wind speed across the weather stations near Sydney ranges from 2.1 m/s to 5.7 m/s. Station SA experiences the highest mean wind speed of 5.7 m/s, while station CP has the lowest mean wind speed of 2.1 m/s. In general, wind speed values hover around 3 m/s across most weather stations, except for SA, where the wind speed is almost two times higher. The standard deviation values of wind speed range from 1.2 m/s in TH to 2.7 m/s in SA, indicating that variations in wind speed are not solely dependent on the distance from the coast but may be influenced by specific wind patterns associated with each station.

Examining the maximum wind speeds, they range from 8.2 m/s to 16.0 m/s, with station SA reporting again the highest value and station CP reporting the lowest one.

Figure 2 illustrates the estimated probability density functions (PDF) of air temperature (left) and wind speed (right) across the weather stations. Each distribution represents the normalized frequency of occurrence of the respective variable. Each Greater Sydney area (east/coast, inner, west) is represented by a different color and different linestyles differentiate the weather stations. The Gaussian kernel density estimation method is employed to calculate the density of the distribution, with a kernel covariance of 0.2 to control the smoothness of the distribution. Analyzing the air temperature distributions reveals a correlation with the territorial partitioning of weather stations. The western suburbs (PL, RM, CN, CP) are represented in red, the inner suburbs (OP, CT, BT, HW) in orange, and the eastern/coastal locations (SA, TH) in blue. Within each group, temperature distributions exhibit similar patterns with slight variations. The western suburbs exhibit lower frequencies of the peak/modal value, which typically falls between 20°C and 25°C, compared to the inner and eastern/coastal stations. Notably, SA and TH display distinct patterns compared to the inner and western suburbs. SA exhibits a higher occurrence of higher temperatures, with a distribution shifted towards higher values. On the other hand, TH has a lower modal value that does not exceed 20°C, and its bell-shaped distribution is narrower, indicating less variability. Focusing on wind speed distributions, greater variability and no clear correlation with territorial partitioning are observed. Station SA demonstrates higher values and greater variability in wind speeds, while station PL exhibits lower values and reduced variability.

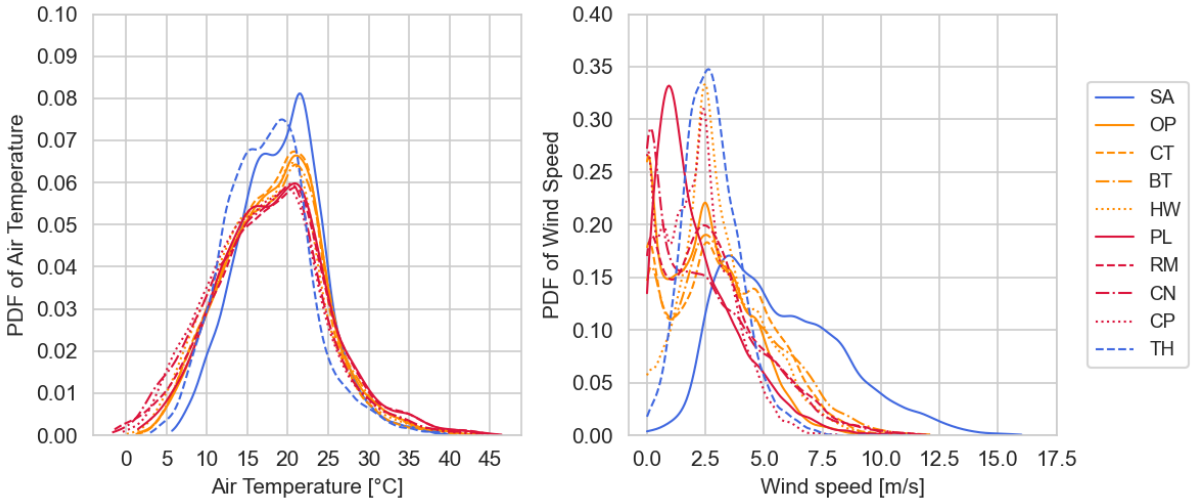

Figure 2: Probability density function (PDF) of the air temperature (left) and wind speed (right) across the weather stations

Figure 3 illustrates the annual Cooling Degree Hours (CDH) calculated using a base temperature of 19.5°C. CDH represents the cumulative sum of hourly (positive) temperature differences from the base temperature over the course of the year. The resulting cooling degree hours (CDHs) range from a minimum of 11,054 at TH to a maximum of 19,568 in PL for the period 2016-2017. There is no discernible pattern related to territorial partitioning, and the spatial variation of CDHs is likely influenced by topographic factors (urban form, vegetation, proximity to water bodies). However, the

western stations of RM and PL exhibit the highest CDH values, while the eastern TH station shows nearly half of the CDH values. These findings align with previous studies conducted during the period 2015-2016 [24].

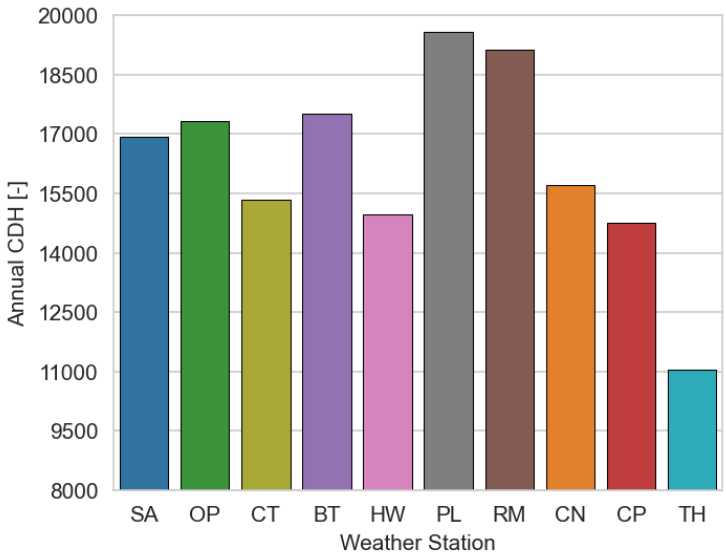

Figure 3: Annual CDH for each weather station

3.2 PV operating cell temperatures and performance metrics

This section focuses on photovoltaic (PV) operating cell temperatures predictions and the associated performance metrics. It investigates the influence of mounting configurations and local climate conditions on PV cell temperatures, highlighting the adverse impact of high temperature conditions on PV electrical performance.

3.2.1 PV operating cell temperatures across weather stations and mounting configurations

Figure 4 presents the boxplot depicting the distribution of PV cell operating temperature estimations across different weather stations and mounting configurations, namely open rack glass/cell/polymer (ORgp), open rack glass/cell/glass (ORgg), close roof mount glass/cell/glass (CMgg), and insulated back glass/cell/polymer (IBgp). The median value of PV cell operating temperature varies across configurations, ranging from approximately 30°C for open rack configurations to about 35°C for close roof and insulated back configurations. Nevertheless, close roof and insulated back configurations exhibit higher variability compared to the two open rack configurations, with the 75th percentile reaching up to 50°C, approximately 10°C higher than open rack.

The maximum values for the open rack configurations fall within the range of 65°C to 70°C, while close roof mount ranges between 80°C and 90°C. The insulated back configuration can reach even higher temperatures, ranging from 90°C to 100°C.

Across weather stations, no significant differences are observed, except for station SA, which exhibits lower variability and a lower frequency of extremely high temperatures. This can be attributed to the beneficial effect of substantially higher wind speeds at that particular site.

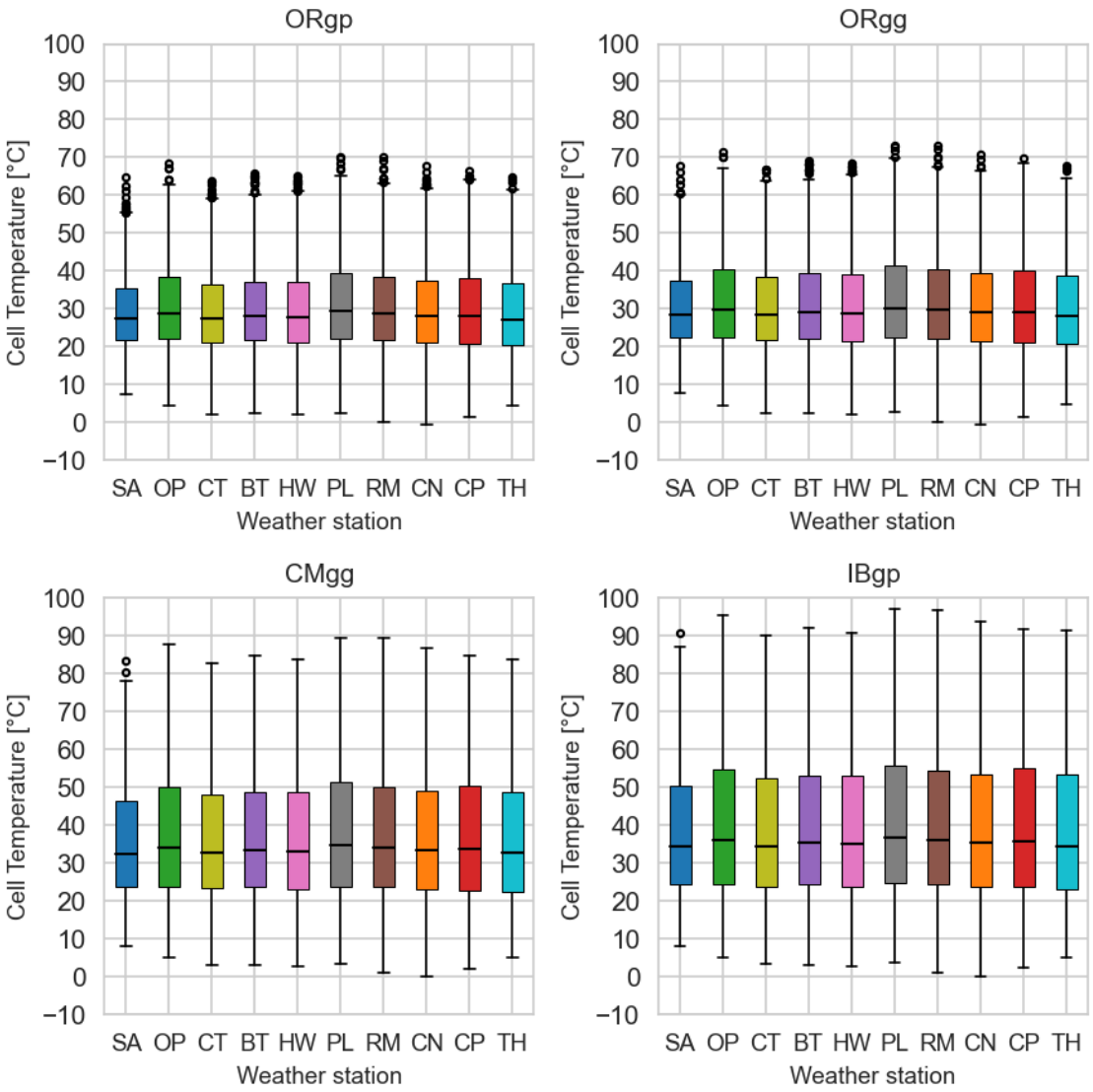

Figure 4: PV cell operating temperatures across the weather stations and mounting configurations. Each graph represents a different mounting configuration whereas each weather station has a different colour

Observing the mean PV cell temperatures across the stations over the entire period, relatively small variations of approximately 2-3°C are observed. However, a significant positive linear relationship (R-Pearson ranging from 0.76 to 0.79) emerges between the mean values and the distance from the nearest coast, as depicted in Figure 5. This relationship suggests that as the distance from the coast increases, the mean PV cell temperatures tend to rise.

It is worth noting that station OP deviates from this trend. Despite having similar air temperatures to other inner stations such as CT, BT, and HW, station OP exhibits higher PV operating cell temperatures.

This anomaly may be attributed to lower wind speed values at station OP, aligning it more closely with the western stations (PL, RM, CN, and CP).
Conversely, the positive influence of sea breeze is once again highlighted by the lower PV cell temperatures observed at stations SA and TH. These stations benefit from the cooling effect of the sea breeze, resulting in lower mean PV cell temperatures compared to other locations.

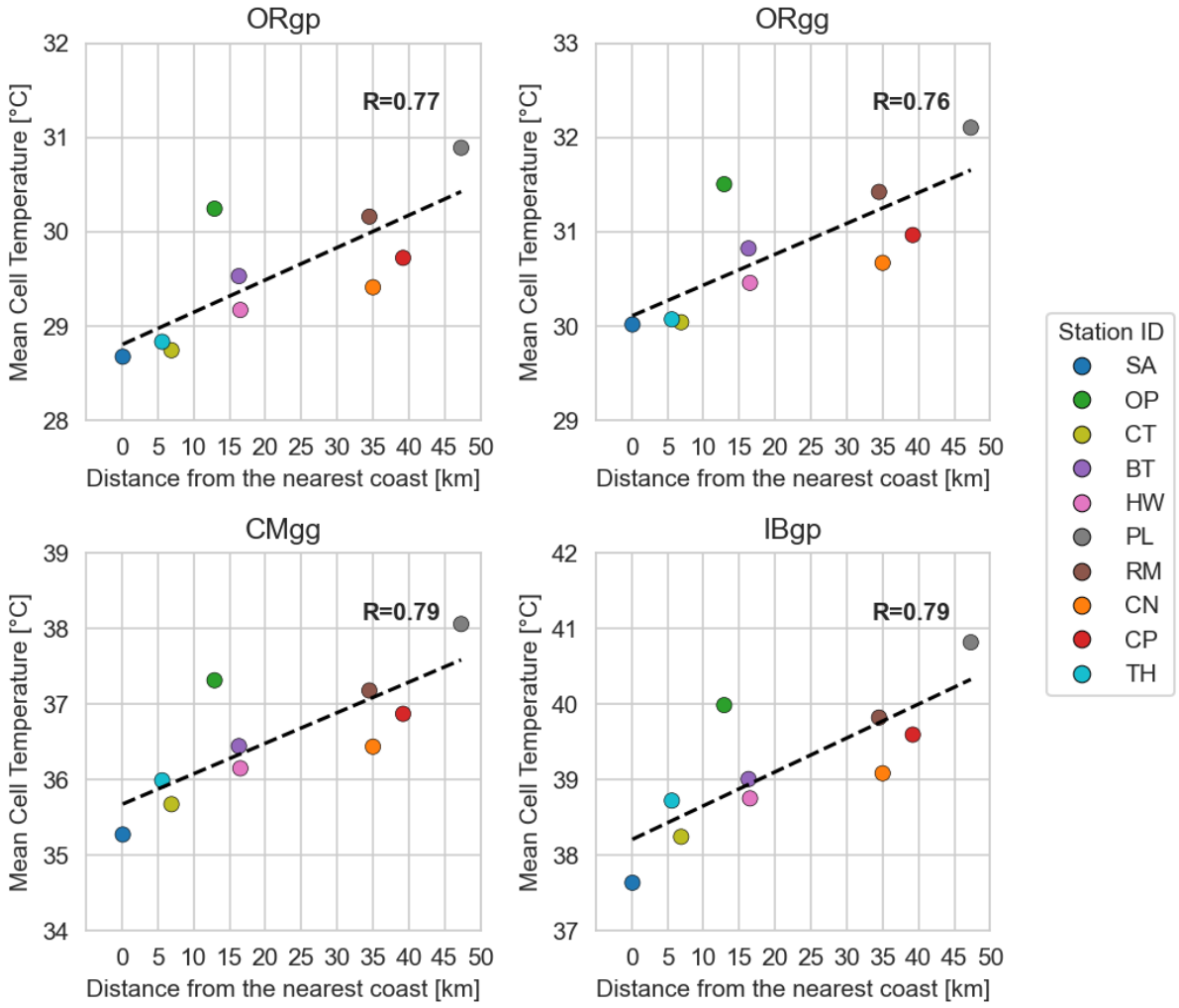

Figure 5: Mean PV cell operating temperatures across the weather stations as a function of the distance from the coast. Each graph represents a different mounting configuration.

Despite overall slight variations in PV operating cell temperatures across the stations over the entire period, analyzing the hourly and monthly patterns reveals more significant differences. In Figure 6, the average (solid line) and maximum (dotted line) standard deviation across the ten weather stations are plotted for each hour of the day. The months of January (representing the summer period, shown in red) and July (representing the winter period, shown in blue) are shown for the sake of clarity.
It is observed that PV operating cell temperature variability is minimal in winter but becomes more pronounced during the central hours of the day in summer when solar radiation values are higher. The maximum standard deviation values range from 7 to over 8°C around midday, with average standard

deviation values between 3 and 4°C. This demonstrates the significant impact of solar radiation on PV cell temperature variability.

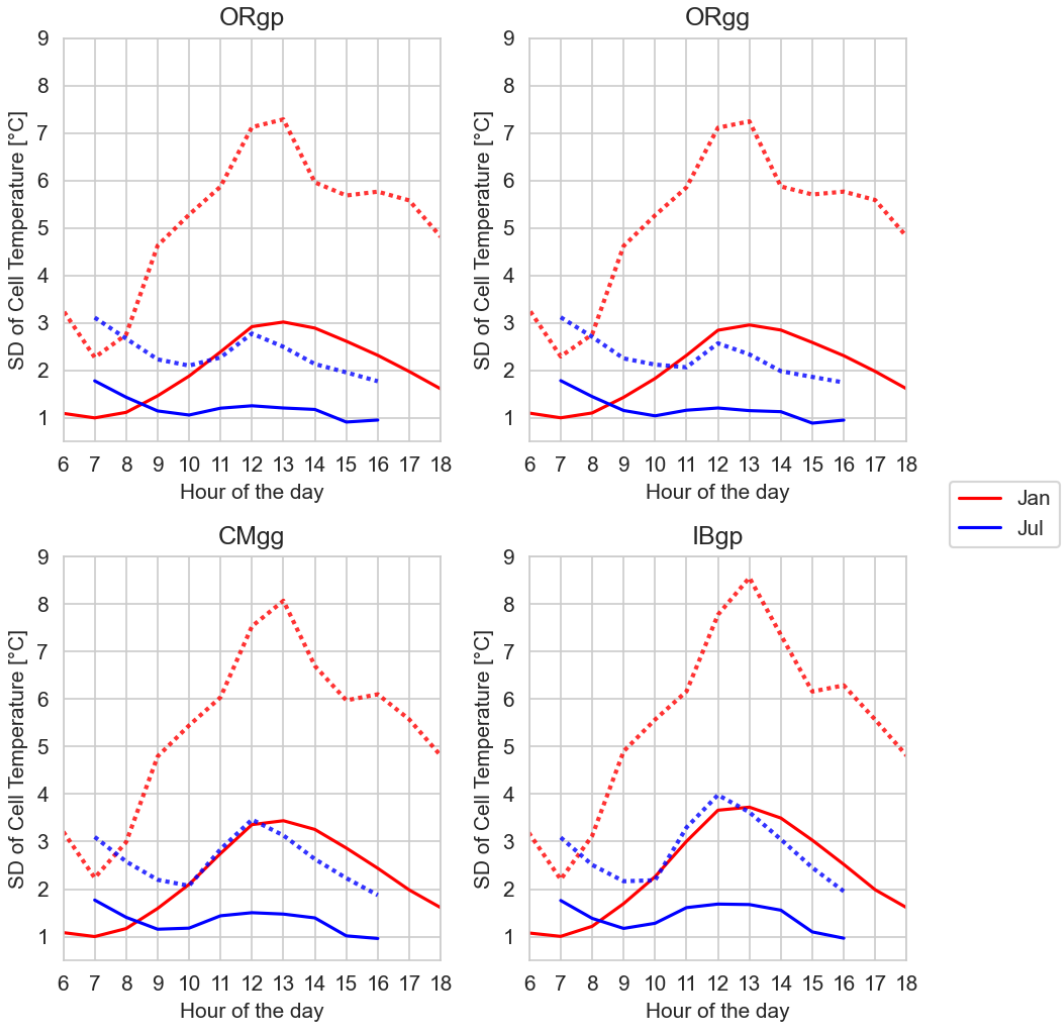

Figure 6: Average (solid line) and maximum (dotted line) standard deviation of PV operating cell temperatures across the weather stations for each hour of the day during summer (January) and winter (July).

The temperature analysis revealed variations in PV cell operating temperatures across weather stations and mounting configurations, with close roof and insulated back mount configurations exhibiting significantly higher temperatures and greater variability compared to open rack configurations. Additionally, meaningful variations in PV cell operating temperatures among weather stations are observed particularly during summer. Based on these findings, the next section is dedicated to the the impact of high cell operating temperatures on the selected PV performance metrics.

3.2.2 Effects of high temperatures on performance metrics

Figure 7 shows the monthly Performance Ratio (PR) for the four different mounting configurations, namely open rack glass/cell/polymer (ORgp), open rack glass/cell/glass (ORgg), close roof mount glass/cell/glass (CMgg), and insulated back glass/cell/polymer (IBgp), across the ten weather stations. Each diagram represents a specific mounting configuration, while each weather station is indicated by a distinct colour. The highest PR values are observed in July (winter), with average values across all weather stations ranging from 0.93 for the two open rack configurations (ORgg and ORgp) to 0.89 for the close roof mount (CMgg) and 0.88 for the insulated back (IBgp). During the winter months, the differences in PR across the weather stations are minimal, with variances of around 1%. In contrast, the lowest PR values are recorded in November (summer). On average, across all weather stations, the PR

values in November range from 0.88 and 0.87 for ORgp and ORgg respectively, to 0.82 for CMgg and 0.80 for IBgp. Notably, the variations across the weather stations are more substantial during this period, with differences ranging from 3.5% for the open rack configurations to 5.0% for the insulated back, comparing the best site (Sydney Airport, SA) to the worst one (Penrith Lakes, PL).

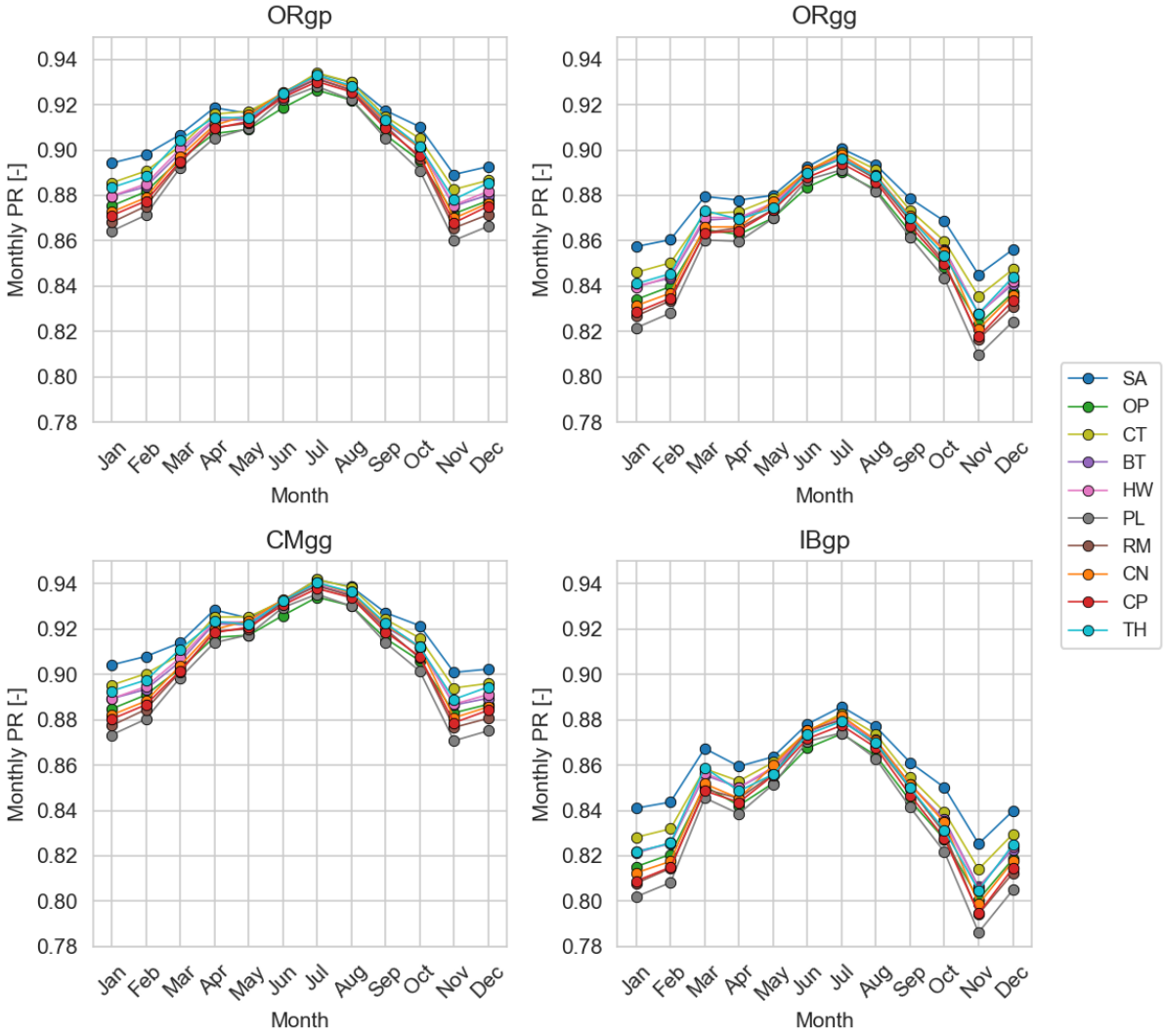

Figure 7: Monthly Performance Ratio (PR) across the weather stations and mounting configurations.

To further investigate the impact of high temperatures on both PV system performance and cooling demand during the summer months (December to February), the daily performance ratio (PR) is calculated for all the weather stations. The calculated daily PR values are then plotted against the cumulated daily values of Cooling Degree Hours (CDH), with a colour gradient used to represent the levels of daily total solar radiation reaching the PV surface expressed in Wh/(m^2day). The results are shown in Figure 8, with each scatterplot representing a different mounting configuration. The black line in the figure evidence a negative exponential relationship between the two variables, with a coefficient of correlation (R^2) ranging from 0.49 for the IBgp configuration to 0.67 for the ORgp configuration. Higher CDH, indicating a greater cooling demand, correspond to a decrease in the PV performance ratio. The PR varies from a minimum value of about 0.80 for the open rack configurations to about 0.70 for the insulated back configuration. This decrease is particularly evident on days with high irradiances, where the potential for energy conversion is high, but the PV performance is significantly reduced, leading to a maximum decrease of PR values up to 0.20-0.30.

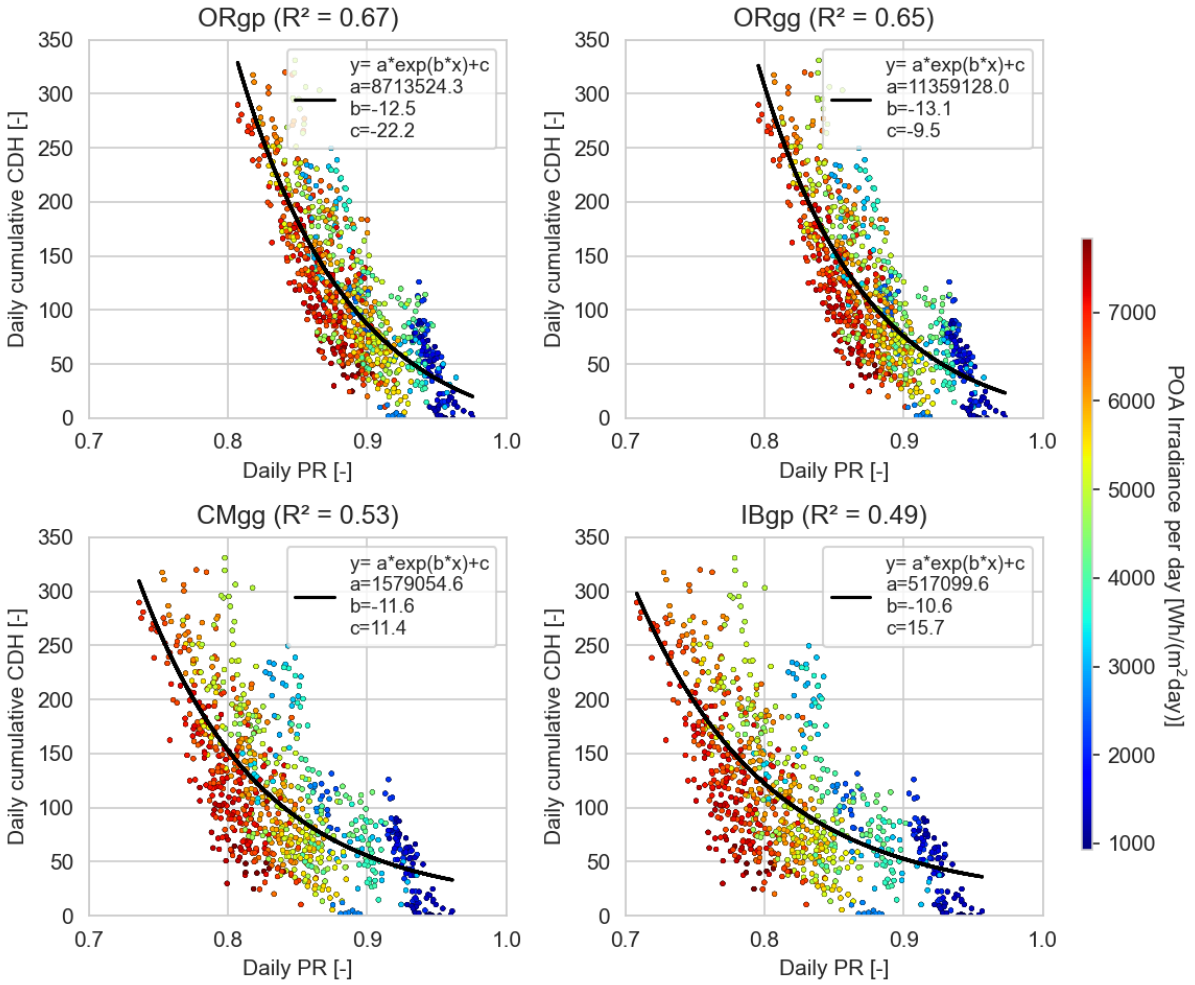

Figure 8: Exponential relationship between daily performance ratio (PR) and cumulative daily Cooling Degree Hours (CDH) across all weather stations during the summer months (December to February). Each diagram represents a different mounting configuration and the colour bar displays the daily total solar energy reaching the PV surface.

Figure 9 presents the average hourly values of photovoltaic (PV) efficiency in November (left) and July (right) across all weather stations. These two months were chosen to represent the best and worst PV performance periods. The plots compare the performance of the best-case scenario (open rack glass/cell/polymer, ORgp) and the worst-case scenario (insulated back glass/cell/polymer, IBgp), indicated by solid and dashed lines, respectively.

As observed from both graphs, there is a substantial difference in efficiency between the two analysed months, with November exhibiting significantly lower values compared to July. The influence of the mounting configuration is evident in both graphs, with efficiency values lower by approximately 1-2% for the insulated back configuration. Conversely, the impact of local climatic conditions becomes

apparent only in November, particularly during the central hours of the day, where efficiency differences of approximately 1% exist between different weather stations.
During the central hours in November, the minimum efficiency values can drop as low as about 11% compared to the rated efficiency at Standard Test Conditions (STC) of 15.63%.

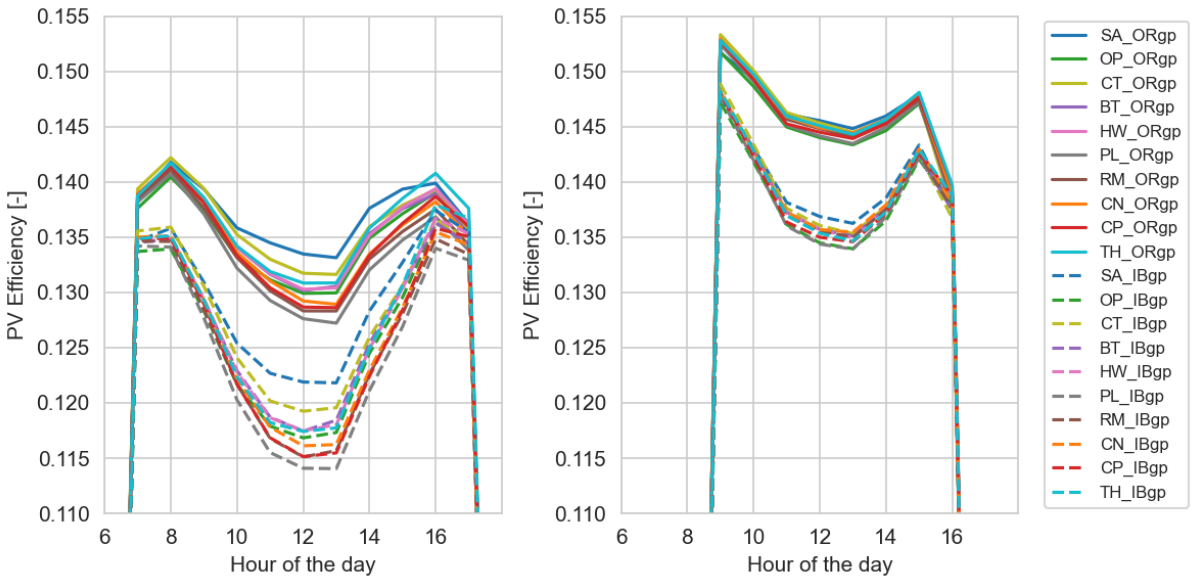

Figure 9:Average hourly values of PV efficiency across the weather stations during November (left) and July (right). Solid and dashed lines are referred to ORgp and IBgp configurations respectively.

Figure 10 shows the relationship between hourly values of normalized efficiency and PV cell operating temperatures. To illustrate the results concisely, only the data for Penrith Lakes (PL) weather station, which experiences the highest temperatures, is presented. For open rack configurations, the cell temperature can reach up to 70°C, resulting in a decline in normalized efficiency to approximately 0.75. In contrast, close roof mount and insulated back configurations exhibit higher cell temperatures, reaching around 90°C and 100°C, respectively, leading to a further reduction in normalized efficiency, to less than 0.65.
The diagram also reveals that at an operating cell temperature of approximately 25°C, which corresponds to the standard test temperature, and during periods of low irradiance levels (<250 W/m^2), the normalized efficiency shows greater variability. This variability is primarily related to the angular effect, which is most prominent during sunrise and sunset hours.

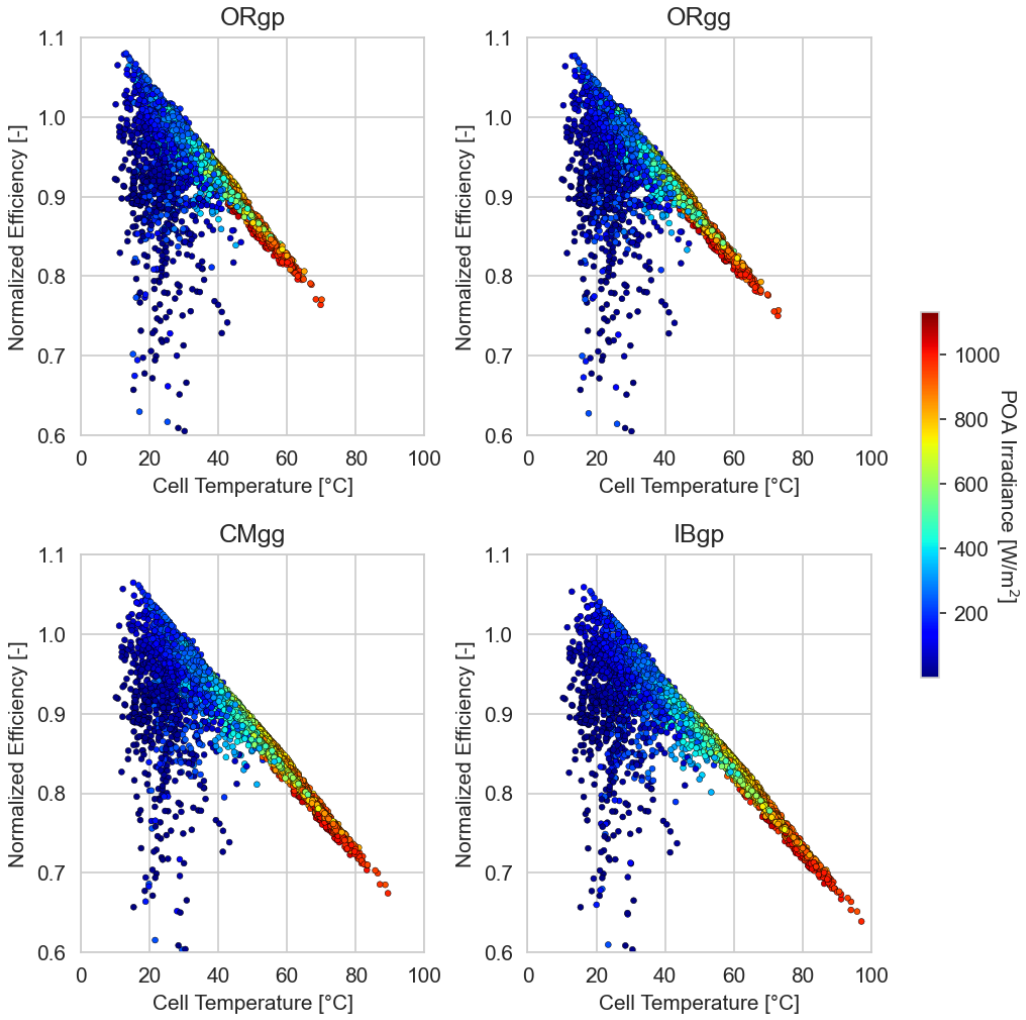

Figure 10: Normalized efficiency and PV cell operating temperature for Penrith Lakes (PL) weather station. Each diagram represents a different mounting configuration.

3.2.3 Power losses due to temperature

The power losses due to temperature ($P^*_{loss,T}$) quantify the deviation of PV power output from the standard test cell temperature conditions (T_c=25°C). The yearly average $P^*_{loss,T}$ is calculated for each weather station and mounting configuration. As expected, the insulated back configuration (IBgp) exhibits the highest temperature losses, with an average yearly value of approximately -10%, compared to -8% for the close roof mount configuration (CMgg). In contrast, the open rack configurations (ORgp and ORgg) demonstrate significantly lower temperature losses, generally below -5%. Among the weather stations, the impact of temperature is more pronounced in the western stations of PL, RM, and CP, as well as in the inner station of OP, which experiences lower wind speeds compared to other inner stations. Conversely, station SA, located on the coast, is the least affected, despite higher ambient temperatures, due to the beneficial effect of the sea breeze.

Observing the daily average $P^*_{loss,T}$ (averaged across all weather stations), which are plotted in Figure 11, it is evident that during extremely hot days from November to February, the daily average $P^*_{loss,T}$ can reach values as low as approximately -35%.

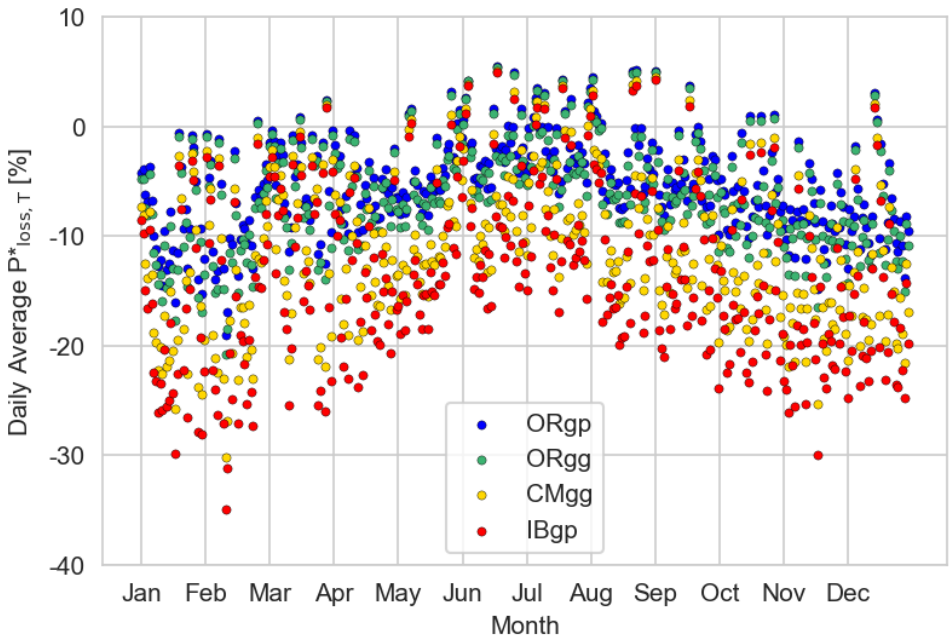

Figure 11: Daily average $P^*_{loss,T}$ (average values across all weather stations) across the mounting configurations identified by different colours.

Focusing on the worst case scenario, specifically the insulated back configuration under Penrith Lakes (PL) local climate conditions, the results indicate that the hourly values of $P^*_{loss,T}$ can reach up to -50%, which represent the highest temperature derating observed in this study. This phenomenon is predominantly observed during the summer months and the central hours of the day when PV output power reaches its peak.

Considering a threshold value of -20%, the number of hours where $P^*_{loss,T}$ falls below this threshold is 2, 11, 392, and 884 for ORgp, ORgg, CMgg, and IBgp configurations, respectively. Taking into account the total number of operating hours for PV systems, which is approximately 3700, this implies that power loss due to temperature significantly affects PV production for 0.1%, 0.3%, 10.7%, and 24.0% of the time for ORgp, ORgg, CMgg, and IBgp configurations, respectively.

3.2.4 Impact of local climate and mounting configuration on PV production

Figure 12 presents the average monthly PV energy production in kWh/(m²month) across all weather stations for different mounting configurations, distinguished by different colours. Error bars are included to illustrate the percentage difference in average monthly PV energy production between the least and most productive weather station. The impact of local climate conditions is particularly evident from November to February and for the close roof mount and insulated back configurations, as indicated by the error bars. The highest percentage difference is observed in January for the insulated back configuration, reaching a maximum value of 5.7%. Conversely, the lowest values are observed from May to July, where the impact of local climate conditions is minimal (approximately 1% in July). The mounting configuration also plays a significant role, especially during the hottest months. Across all weather stations, the ORgp configuration exhibits the highest power production, benefiting from lower temperatures. On the other hand, the least productive configuration is IBgp, which experiences a monthly power production decrease compared to ORgp ranging from a minimum of 7.6% in March to a maximum of 10.6% in November.

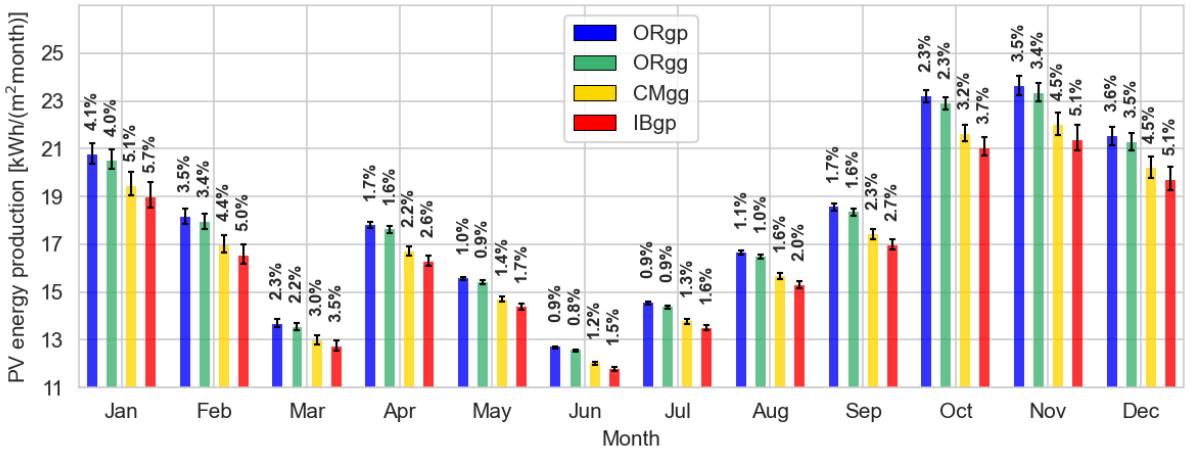

Figure 12: Monthly PV power production (average across weather stations) as a function of the mounting configuration identified by the different colours. Error bars represent the maximum percentage difference of PV energy production across the weather stations.

3.3 Daytime convection and radiation

This section presents the results regarding the daytime convective and radiative heat fluxes released by PV modules for the open rack glass/cell/polymer and close roof mount glass/cell/glass configurations. The aim is to analyse the impact of local climatic conditions on these fluxes.

Figure 13 shows the histograms of the convective flux values across all weather stations for the two analysed configurations (open rack, OR, and close roof mount, CM), along with the mean, median, and standard deviation values for the warm period (left), which spans from October to March, and the cool period (right), from April to September.

As observed from the graphs, despite the temperature differences in the PV cells highlighted in the previous sections, the differences between the two configurations are slight. The open rack configuration exhibits, according to the present model, slightly higher values compared to CM, especially for higher flux values. The mean, median, and standard deviation values are very similar for both configurations. During the warm period, the average convective flux is slightly higher (around 170-180 W/m^2) compared to the cool period, which hovers around 150 W/m^2. In the warm period, the maximum values for the CM configuration do not exceed 550 W/m^2, while for the OR configuration, they reach peaks of approximately 700 W/m^2.

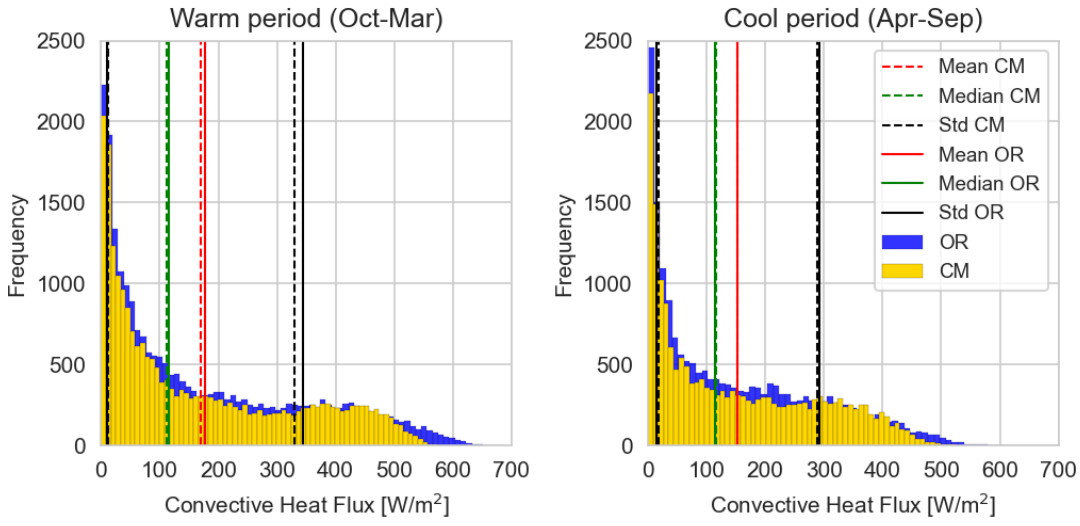

Figure 13: Histogram of the convective heat fluxes across all weather stations during the warm (left) and the cool (right) periods for the two considered mounting configurations (open rack, OR, and close roof mount, CM). Mean, median, and standard deviation values are represented by the red, green, and black lines respectively.

Table 6 summarizes the total convective energy in kWh/m^2 released by open rack (OR) and close roof (CM) installed PV modules over the warm and the cool periods across all ten weather stations. The table also includes the percentage difference calculated between the CM and OR configuration values. The data reveals noticeable variations among the weather stations. In both periods, the highest values are observed at Sydney Airport (SA) station, with average values ranging from 480 kWh/m^2 during the warm period to around 340 kWh/m^2 during the cool period. On the other hand, the lowest values are observed at Penrith Lakes (PL) station, ranging from 380 kWh/m^2 in the warm period to 260 kWh/m^2 in the cool period, resulting in a percentage difference of approximately -22% compared to SA.
Interestingly, during the warm period, in most weather stations the present model exhibits a negative percentage difference between the CM and OR configurations, indicating a decrease in the total convective energy released by the close roof mount configuration. However, this trend does not hold for the PL, CP, and TH stations. This trend becomes even more pronounced during the cool period, particularly at the PL station, where the total convective energy released by the close roof mount configuration is 8.4% higher than the open rack configuration. This observation can be attributed to local climatic conditions, particularly wind speed. As seen in previous sections, the PL station experiences higher PV cell temperatures primarily due to lower wind speeds at the site (which is located in the western part of the Greater Sydney area), which hinder effective cooling compared to areas closer to the coast. The reduced air circulation around the modules diminishes the convective heat flux, impeding module cooling. As a result, the higher PV cell temperatures in the close roof mount configuration lead to an increased convective heat flux compared to the open rack configuration due to the larger temperature difference between the cells and the surrounding air. In most other weather stations, where wind speed values are higher, air circulation is favoured, especially in the open rack configuration, resulting in greater convective heat release compared to CM, despite lower cell temperatures.

Table 6: Total Convective Energy released by open rack (OR) and close roof (CM) installed PV modules across the selected weather stations (WS) during the warm and the cool periods.

Total Convective Energy [kWh/m^2]						
	Warm (Oct-Mar)			**Cool (Apr-Sept)**		
WS	**OR**	**CM**	**% diff**	**OR**	**CM**	**% diff**
SA	512.1	454.2	-11.3%	357.8	328.1	-8.3%
OP	419.1	406.4	-3.0%	282.5	288.1	2.0%
CT	459.5	427.7	-6.9%	312.0	303.7	-2.6%
BT	454.8	425.1	-6.5%	312.8	304.2	-2.7%
HW	445.6	420.5	-5.6%	306.1	300.5	-1.8%
PL	376.0	384.9	2.3%	249.0	270.0	8.4%
RM	421.4	408.4	-3.1%	289.8	291.7	0.6%
CN	416.0	404.0	-2.9%	287.1	289.5	0.8%
CP	390.9	392.4	0.4%	279.2	286.6	2.6%
TH	392.1	392.9	0.2%	270.4	282.2	4.4%

The variation of wind speed values has a discernible impact on the relative significance of changes in radiative and convective heat transfer, as shown in Figure 14. The graph presents the proportional contributions of radiative and convective heat transfer to the overall heat transfer, as a function of wind speed and net irradiance incident on the PV surface (i.e., total irradiance minus the reflected component from the front PV glass). For conciseness, the results are specifically displayed for the close roof mount configuration in the Penrith Lakes (PL) local climate conditions, although similar patterns are observed across other weather stations and mounting configurations. At low wind speeds (<2 m/s), convection

accounts for only 30-40% of the total heat transfer, while at 10 m/s, its contribution increases to approximately 60%. Beyond approximately 3-6 m/s, the convective heat transfer process is the dominant mode.

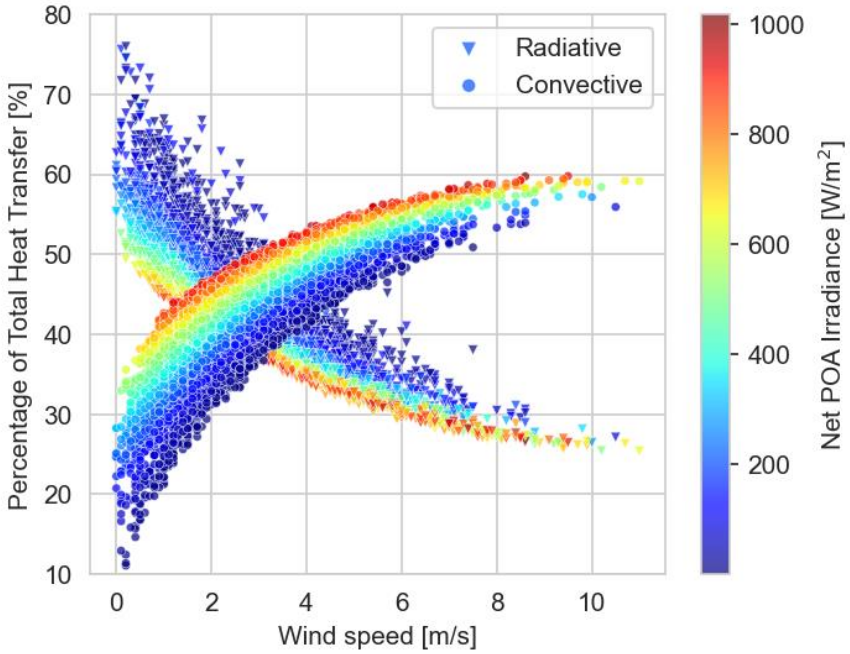

Figure 14: Radiative and convective heat transfers as a percentage of total heat transfer at various wind speeds. The results are referred to close roof mount under Penrith Lakes (PL) climate conditions.

The analysis of convective and radiative heat fluxes in PV modules under different local climate conditions and mounting configurations provides valuable insights into the thermal behaviour of PV systems. Open rack PV modules generally exhibit higher convective heat release compared to close roof mount. This difference is primarily due to lower convective heat transfer at the lower side of tilted roofs, as opposed to open rack systems with free air flow on both sides. The higher convective heat flux in open rack configurations corresponds to lower PV cell temperatures and increased power output. Conversely, close roof installations experience lower convective heat flux due to limited air circulation, resulting in higher PV cell temperatures. Nonetheless, the impact of wind speed is critical in this context. At sites characterized by low wind speeds (<2 m/s), the relative contribution of convective heat transfer to the overall heat transfer is approximately half that observed at wind speeds around 10 m/s. Consequently, this circumstance may cause higher convective heat transfer in close roof mount configurations, primarily due to high PV cell temperatures.

4. Conclusions and future perspectives

Given the growing importance of urban-integrated PV systems, accurate electrical and thermal models are essential for predicting their performance under local climate conditions characterized by high temperatures and exacerbated by urban overheating and extreme climate events. The study analysed the electrical and thermal performance of four PV configurations (open rack glass/cell/polymer, open rack glass/cell/glass, close roof mount glass/cell/glass, and insulated back glass/cell/polymer) using local climatic data recorded between 2016 and 2017 from ten weather stations in Greater Sydney. The present study relies on dedicated modelling based also on Sandia set of equations. Variations in mounting configurations resulted in significant differences in PV operating cell temperature, with up to 30°C variation between open rack and insulated back setups. Cell temperature variations of approximately 8°C were observed across weather stations, particularly during midday hours and summer months. High temperatures negatively affected performance metrics, leading to power losses of up to -50% compared to standard test temperatures. Local climate conditions and mounting configurations caused variations

of approximately 6% and 11% in PV energy output, respectively. Daytime convective and radiative heat flux analysis highlighted the influence of wind, with higher convective heat flux in open rack configurations but a potential reversal under low wind speed conditions.

Based on the findings, it is evident that the decline in PV performance is directly related to the level of PV system integration. Furthermore, under low wind speed conditions, roof-mounted systems exhibited lower electrical performance and potentially higher convective heat release.

This study provides valuable insights into the thermal behaviour of PV systems in urban contexts characterized by hot weather conditions and exhibiting substantial local climate variations due to overheating. Significant variations are observed within the same metropolitan area, emphasizing the importance of acquiring local data. The study findings may be of interest especially for densely populated European metropolitan areas which are often characterized by a very limited number of local weather stations which are generally located far from urban centres. Concerning Sydney case study, the results show that PV performance in western suburbs is significantly affected by power losses due to temperature, highlighting the need of prioritizing the implementation of adequate urban planning and development strategies (cooling techniques for PV systems, climate mitigation strategies as cool roofs, green roofs).

Limitations of this study include the use of local climate data from non-urban weather stations, potentially underestimating the impact of urban overheating on PV performance, and the exclusion of other meteorological parameters like rainfall that can cool PV modules. Furthermore, it should be noted that this type of study may be particularly relevant for densely populated metropolitan areas with a hot climate. The study focused on daytime heat fluxes and did not consider the impact of PVs on rooftop heat balance, highlighting the need for rooftop modelling to accurately quantify the influence of PVs in the urban environment. Additionally, while the King's temperature model used in this study is valuable for predicting PV cell temperatures during daytime, it is not able to account for cooling below ambient air temperatures at night, which is relevant for urban heat island studies.

In conclusion, accurate modelling incorporating local climate conditions and mounting configurations is crucial for understanding the electrical and thermal behaviour of urban-integrated PV systems. The results emphasize their effects on PV operating cell temperature, power production, and convective heat flux. Future research should address these limitations by incorporating rooftop modelling, improving temperature models, and evaluating PVs' actual impact on urban overheating.

5. Acknowledgements

Authors thank the CNRS for supporting this work through the International Research Project Naturban. The research unit LOCIE is a member of the INES Solar Academy Research Center.

References

[1] M. Santamouris, Analyzing the heat island magnitude and characteristics in one hundred Asian and Australian cities and regions, Sci. Total Environ. 512–513 (2015) 582–598. https://doi.org/10.1016/j.scitotenv.2015.01.060.

[2] T.R. Oke, The energetic basis of the urban heat island, Q. J. R. Meteorol. Soc. 108 (1982) 1–24. https://doi.org/10.1002/qj.49710845502.

[3] M. Kumar, S.C. Bhan, A. Tyagi, R. Magotra, Y. Sharma, Review of Urban Heat Islands: Monitoring, Forecast and Impacts, VayuMandal. 47 (2021) 2021. https://www.researchgate.net/publication/357528081.

[4] P.A. Mirzaei, Recent challenges in modeling of urban heat island, Sustain. Cities Soc. (2015). https://doi.org/10.1016/j.scs.2015.04.001.

[5] A. Boccalatte, M. Fossa, M. Thebault, J. Ramousse, C. Ménézo, Mapping the urban heat Island at the territory scale: An unsupervised learning approach for urban planning applied to the Canton of Geneva, Sustain. Cities Soc. 96 (2023) 104677. https://doi.org/10.1016/j.scs.2023.104677.

[6] A. Boccalatte, M. Fossa, L. Gaillard, C. Menezo, Microclimate and urban morphology effects on building energy demand in different European cities, Energy Build. 224 (2020) 110129. https://doi.org/10.1016/j.enbuild.2020.110129.

[7] A. Boccalatte, M. Thebault, C. Ménézo, J. Ramousse, M. Fossa, Evaluating the impact of urban morphology on rooftop solar radiation: A new city-scale approach based on Geneva GIS data, Energy Build. 260 (2022) 111919. https://doi.org/10.1016/j.enbuild.2022.111919.

[8] H.S. Khan, M. Santamouris, R. Paolini, P. Caccetta, P. Kassomenos, Analyzing the local and climatic conditions affecting the urban overheating magnitude during the Heatwaves (HWs) in a coastal city: A case study of the greater Sydney region, Sci. Total Environ. 755 (2021) 142515. https://doi.org/10.1016/j.scitotenv.2020.142515.

[9] D. Habeeb, J. Vargo, B. Stone, Rising heat wave trends in large US cities, Nat. Hazards. 76 (2015) 1651–1665. https://doi.org/10.1007/s11069-014-1563-z.

[10] F. Nadeem, S. Tariq, Z.U. Haq, H.S. Khan, Investigating the synergies between the Urban Heat Island (UHI) and Heatwaves (HWs), Prepr. Environ. Sci. Pollut. Res. (2022) 1–32.

[11] J.A. Principe, W. Takeuchi, Assessment of solar PV power potential in the Asia Pacific region with remote sensing considering the effects of high temperature, dust and snow, Int. Arch. Photogramm. Remote Sens. Spat. Inf. Sci. - ISPRS Arch. 42 (2019) 339–346. https://doi.org/10.5194/isprs-archives-XLII-4-W19-339-2019.

[12] S.C. Lewis, A.D. King, D.M. Mitchell, Australia's Unprecedented Future Temperature Extremes Under Paris Limits to Warming, Geophys. Res. Lett. 44 (2017) 9947–9956. https://doi.org/10.1002/2017GL074612.

[13] M. Dhimish, A. Alrashidi, Photovoltaic degradation rate affected by different weather conditions: A case study based on pv systems in the uk and australia, Electron. 9 (2020). https://doi.org/10.3390/electronics9040650.

[14] H. Outhred, M. Retnanestri, Insights from the Experience with Solar Photovoltaic Systems in Australia and Indonesia, Energy Procedia. 65 (2015) 121–130. https://doi.org/10.1016/j.egypro.2015.01.044.

[15] L. Koschier, R. Egan, National Survey Report of PV Power Applications in Australia 2021, 2021.

[16] A.J. Chapman, B. McLellan, T. Tezuka, Residential solar PV policy: An analysis of impacts, successes and failures in the Australian case, Renew. Energy. 86 (2016) 1265–1279. https://doi.org/10.1016/j.renene.2015.09.061.

[17] Y. Ma, S.C. Saha, W. Miller, L. Guan, Comparison of different solar-assisted air conditioning systems for Australian office buildings, Energies. 10 (2017). https://doi.org/10.3390/en10101463.

[18] S.E. Perkins, L. V. Alexander, J.R. Nairn, Increasing frequency, intensity and duration of observed global heatwaves and warm spells, Geophys. Res. Lett. 39 (2012) 1–5. https://doi.org/10.1029/2012GL053361.

[19] W.W. Ma, M.G. Rasul, G. Liu, M. Li, X.H. Tan, Climate change impacts on techno-economic performance of roof PV solar system in Australia, Renew. Energy. 88 (2016) 430–438. https://doi.org/10.1016/j.renene.2015.11.048.

[20] A. Dhoke, A. Mengede, Degradation analysis of PV modules operating in Australian environment, 2017 Australas. Univ. Power Eng. Conf. AUPEC 2017. 2017-Novem (2018) 1–5. https://doi.org/10.1109/AUPEC.2017.8282420.

[21] J. Potgieter, N. Nazarian, M.J. Lipson, M.A. Hart, G. Ulpiani, W. Morrison, K. Benjamin, Combining High-Resolution Land Use Data With Crowdsourced Air Temperature to Investigate Intra-Urban Microclimate, Front. Environ. Sci. 9 (2021) 1–19. https://doi.org/10.3389/fenvs.2021.720323.

[22] G.Y. Yun, J. Ngarambe, P.N. Duhirwe, G. Ulpiani, R. Paolini, S. Haddad, K. Vasilakopoulou, M. Santamouris, Predicting the magnitude and the characteristics of the urban heat island in coastal cities in the proximity of desert landforms. The case of Sydney, Sci. Total Environ. 709 (2020) 136068. https://doi.org/10.1016/j.scitotenv.2019.136068.

[23] I. Livada, A. Synnefa, S. Haddad, R. Paolini, S. Garshasbi, G. Ulpiani, F. Fiorito, K. Vassilakopoulou, P. Osmond, M. Santamouris, Time series analysis of ambient air-temperature during the period 1970–2016 over Sydney, Australia, Sci. Total Environ. 648 (2019) 1627–1638. https://doi.org/10.1016/j.scitotenv.2018.08.144.

[24] M. Santamouris, S. Haddad, F. Fiorito, P. Osmond, L. Ding, D. Prasad, X. Zhai, R. Wang, Urban heat island and overheating characteristics in Sydney, Australia. An analysis of multiyear measurements, Sustain. 9 (2017). https://doi.org/10.3390/su9050712.

[25] H.S. Khan, R. Paolini, M. Santamouris, P. Caccetta, Exploring the synergies between urban overheating and heatwaves (HWS) in western Sydney, Energies. 13 (2020) 1–17. https://doi.org/10.3390/en13020470.

[26] P. Vaneckova, P.J. Beggs, R.J. de Dear, K.W.J. McCracken, Effect of temperature on mortality during the six warmer months in Sydney, Australia, between 1993 and 2004, Environ. Res. 108 (2008) 361–369. https://doi.org/10.1016/j.envres.2008.07.015.

[27] M. Santamouris, S. Haddad, M. Saliari, K. Vasilakopoulou, A. Synnefa, R. Paolini, G. Ulpiani, S. Garshasbi, F. Fiorito, On the energy impact of urban heat island in Sydney: Climate and energy potential of mitigation technologies, Energy Build. 166 (2018) 154–164. https://doi.org/10.1016/j.enbuild.2018.02.007.

[28] H.D. and T.T. Matthew Adams, Impacts of land-use change on Sydney's future temperatures, Off. Environ. Heritage,. (2015).

[29] M. Mehdi, N. Ammari, A. Alami Merrouni, H. El Gallassi, M. Dahmani, A. Ghennioui, An experimental comparative analysis of different PV technologies performance including the influence of hot-arid climatic parameters: Toward a realistic yield assessment for desert locations, Renew. Energy. 205 (2023) 695–716. https://doi.org/10.1016/j.renene.2023.01.082.

[30] N. Haghdadi, J. Copper, A. Bruce, I. Macgill, Operational performance analysis of distributed PV systems in Australia, Asia-Pacific Sol. Res. Conf. (2016).

[31] S.M. Hashim, R.I. Hassan, Impact of high temperature on PV productivity in hot desert climates, Green Technol. Resilience, Sustain. 2 (2022). https://doi.org/10.1007/s44173-022-00009-9.

[32] T. Huld, R. Gottschalg, H.G. Beyer, M. Topič, Mapping the performance of PV modules, effects of module type and data averaging, Sol. Energy. 84 (2010) 324–338. https://doi.org/10.1016/j.solener.2009.12.002.

[33] J.K. Kaldellis, M. Kapsali, K.A. Kavadias, Temperature and wind speed impact on the efficiency of PV installations. Experience obtained from outdoor measurements in Greece, Renew. Energy. 66 (2014) 612–624. https://doi.org/10.1016/j.renene.2013.12.041.

[34] C. Tiba, R.E. d. A. Beltrão, Siting PV plant focusing on the effect of local climate variables on electric energy production - Case study for Araripina and Recife, Renew. Energy. 48 (2012) 309–317. https://doi.org/10.1016/j.renene.2012.05.010.

[35] C. Camarena-Gamarra, J. Calle-Maravi, J. Nahui-Ortiz, Benchmarking of Solar PV performance ratio among different regions in Peru: Sample of five small-scale systems., Proc. LACCEI Int. Multi-Conference Eng. Educ. Technol. (2020) 27–31. https://doi.org/10.18687/LACCEI2020.1.1.245.

[36] A.B. Awan, M. Zubair, R.P. Praveen, A.G. Abokhalil, Solar energy resource analysis and evaluation of photovoltaic system performance in various regions of Saudi Arabia, Sustain. 10 (2018) 1–27. https://doi.org/10.3390/su10041129.

[37] S. Garshasbi, A. Khan, M. Santamouris, On the cooling energy penalty of urban photovoltaics: a case study in Sydney, Australia, Energy Build. 294 (2023) 113259. https://doi.org/10.1016/j.enbuild.2023.113259.

[38] J. Siecker, K. Kusakana, B.P. Numbi, A review of solar photovoltaic systems cooling technologies, Renew. Sustain. Energy Rev. 79 (2017) 192–203. https://doi.org/10.1016/j.rser.2017.05.053.

[39] A. Maleki, A. Haghighi, M. El Haj Assad, I. Mahariq, M. Alhuyi Nazari, A review on the approaches employed for cooling PV cells, Sol. Energy. 209 (2020) 170–185. https://doi.org/10.1016/j.solener.2020.08.083.

[40] P. Dwivedi, K. Sudhakar, A. Soni, E. Solomin, I. Kirpichnikova, Advanced cooling techniques of P.V. modules: A state of art, Case Stud. Therm. Eng. 21 (2020) 100674. https://doi.org/10.1016/j.csite.2020.100674.

[41] A.G. Gaglia, S. Lykoudis, A.A. Argiriou, C.A. Balaras, E. Dialynas, Energy efficiency of PV panels under real outdoor conditions–An experimental assessment in Athens, Greece, Renew. Energy. 101 (2017) 236–243. https://doi.org/10.1016/j.renene.2016.08.051.

[42] K. Chumpolrat, V. Sangsuwan, N. Udomdachanut, S. Kittisontirak, S. Songtrai, P. Chinnavornrungsee, A. Limmanee, J. Sritharathikhun, K. Sriprapha, Effect of ambient temperature on performance of grid-connected inverter installed in Thailand, Int. J. Photoenergy. 2014 (2014). https://doi.org/10.1155/2014/502628.

[43] D. Hassan Daher, L. Gaillard, C. Ménézo, Experimental assessment of long-term performance degradation for a PV power plant operating in a desert maritime climate, Renew. Energy. 187 (2022) 44–55. https://doi.org/10.1016/j.renene.2022.01.056.

[44] A.U. Obiwulu, N. Erusiafe, M.A. Olopade, S.C. Nwokolo, Modeling and optimization of back temperature models of mono-crystalline silicon modules with special focus on the effect of meteorological and geographical parameters on PV performance, Renew. Energy. 154 (2020)

404–431. https://doi.org/10.1016/j.renene.2020.02.103.

[45] D. Atsu, I. Seres, M. Aghaei, I. Farkas, Analysis of long-term performance and reliability of PV modules under tropical climatic conditions in sub-Saharan, Renew. Energy. 162 (2020) 285–295. https://doi.org/10.1016/j.renene.2020.08.021.

[46] H. Tebibel, S. Labed, Performance results and analysis of self-regulated PV system in algerian sahara, Renew. Energy. 60 (2013) 691–700. https://doi.org/10.1016/j.renene.2013.06.032.

[47] U. Berardi, J. Graham, Investigation of the impacts of microclimate on PV energy efficiency and outdoor thermal comfort, Sustain. Cities Soc. 62 (2020) 102402. https://doi.org/10.1016/j.scs.2020.102402.

[48] H.J. Solheim, H.G. Fjær, E.A. Sørheim, S.E. Foss, Measurement and simulation of hot spots in solar cells, Energy Procedia. 38 (2013) 183–189. https://doi.org/10.1016/j.egypro.2013.07.266.

[49] M. Dhimish, A. Ahmad, A.M. Tyrrell, Inequalities in photovoltaics modules reliability: From packaging to PV installation site, Renew. Energy. 192 (2022) 805–814. https://doi.org/10.1016/j.renene.2022.04.156.

[50] E. Skoplaki, J.A. Palyvos, Operating temperature of photovoltaic modules: A survey of pertinent correlations, Renew. Energy. 34 (2009) 23–29. https://doi.org/10.1016/j.renene.2008.04.009.

[51] N. Gökmen, W. Hu, P. Hou, Z. Chen, D. Sera, S. Spataru, Investigation of wind speed cooling effect on PV panels in windy locations, Renew. Energy. 90 (2016) 283–290. https://doi.org/10.1016/j.renene.2016.01.017.

[52] M.W. Davis, A.H. Fanney, B.P. Dougherty, Prediction of building integrated photovoltaic cell temperatures, J. Sol. Energy Eng. Trans. ASME. 123 (2001) 200–210. https://doi.org/10.1115/1.1385825.

[53] D.L. King, W.E. Boyson, J.A. Kratochvil, Photovoltaic array performance model, Sandia Rep. No. 2004-3535. 8 (2004) 1–19. https://doi.org/10.2172/919131.

[54] D. Faiman, Assessing the outdoor operating temperature of photovoltaic modules, Prog. Photovoltaics Res. Appl. 16 (2008) 307–315. https://doi.org/10.1002/pip.813.

[55] A.M. Muzathik, Photovoltaic Modules Operating Temperature Estimation Using a Simple Correlation, Int. J. Energy Eng. 4 (2014) 151–158.

[56] E. Skoplaki, A.G. Boudouvis, J.A. Palyvos, A simple correlation for the operating temperature of photovoltaic modules of arbitrary mounting, Sol. Energy Mater. Sol. Cells. 92 (2008) 1393–1402. https://doi.org/10.1016/j.solmat.2008.05.016.

[57] M.K. Fuentes, S. Laboratory, U.S.D. of Energy, A Simplified Thermal Model for Flat-plate Photovoltaic Arrays, Sandia Laboratories, United States, 1987. https://www.osti.gov/biblio/6802914.

[58] R.G. Ross, Interface design considerations for terrestrial solar cell modules, in: 1976.

[59] P. Trinuruk, C. Sorapipatana, D. Chenvidhya, Estimating operating cell temperature of BIPV modules in Thailand, Renew. Energy. 34 (2009) 2515–2523. https://doi.org/10.1016/j.renene.2009.02.027.

[60] M. D'Orazio, C. Di Perna, E. Di Giuseppe, Experimental operating cell temperature assessment of BIPV with different installation configurations on roofs under Mediterranean climate, Renew. Energy. 68 (2014) 378–396. https://doi.org/10.1016/j.renene.2014.02.009.

[61] N. Aoun, Methodology for predicting the PV module temperature based on actual and estimated weather data, Energy Convers. Manag. X. 14 (2022) 100182.

https://doi.org/10.1016/j.ecmx.2022.100182.

[62] M.D. Kempe, D. Holsapple, K. Whitfield, N. Shiradkar, Standards development for modules in high temperature micro-environments, Prog. Photovoltaics Res. Appl. 29 (2021) 445–460. https://doi.org/10.1002/pip.3389.

[63] J. Kurnik, M. Jankovec, K. Brecl, M. Topic, Outdoor testing of PV module temperature and performance under different mounting and operational conditions, Sol. Energy Mater. Sol. Cells. 95 (2011) 373–376. https://doi.org/10.1016/j.solmat.2010.04.022.

[64] D.J. Sailor, J. Anand, R.R. King, Photovoltaics in the built environment: A critical review, Energy Build. 253 (2021) 111479. https://doi.org/10.1016/j.enbuild.2021.111479.

[65] J. Oh, G. TamizhMani, E. Palomino, Temperatures of building applied photovoltaic (BAPV) modules: air gap effects, Reliab. Photovolt. Cells, Modul. Components, Syst. III. 7773 (2010) 777305. https://doi.org/10.1117/12.861069.

[66] Y.F. Nassar, A.A. Salem, The reliability of the photovoltaic utilization in southern cities of Libya, Desalination. 209 (2007) 86–90. https://doi.org/10.1016/j.desal.2007.04.013.

[67] A. Hasan, H. Alnoman, Y. Rashid, Impact of integrated photovoltaic-phase change material system on building energy efficiency in hot climate, Energy Build. 130 (2016) 495–505. https://doi.org/10.1016/j.enbuild.2016.08.059.

[68] J. V. Pham, A. Baniassadi, K.E. Brown, J. Heusinger, D.J. Sailor, Comparing photovoltaic and reflective shade surfaces in the urban environment: Effects on surface sensible heat flux and pedestrian thermal comfort, Urban Clim. 29 (2019). https://doi.org/10.1016/j.uclim.2019.100500.

[69] J. Heusinger, A.M. Broadbent, D.J. Sailor, M. Georgescu, Introduction, evaluation and application of an energy balance model for photovoltaic modules, Sol. Energy. 195 (2020) 382–395. https://doi.org/10.1016/j.solener.2019.11.041.

[70] J. Heusinger, A.M. Broadbent, E.S. Krayenhoff, S. Weber, Adaptation of a photovoltaic energy balance model for rooftop applications, Build. Environ. 192 (2021) 107628. https://doi.org/10.1016/j.buildenv.2021.107628.

[71] R. Pokhrel, A. Walker, J.E. González, A New Methodology to Assess Building Integrated Roof Top Photovoltaic Installations at City Scales: The Tropical Coastal City Case, ASME J. Eng. Sustain. Build. Cities. 1 (2020) 1–11. https://doi.org/10.1115/1.4045347.

[72] G.A. Barron-gafford, R.L. Minor, N.A. Alle, A.D. Cronin, A.E. Brooks, M.A. Pavao-zuckerman, The Photovoltaic Heat Island Effect : Larger solar power plants increase local temperatures, Nat. Publ. Gr. (2016) 1–7. https://doi.org/10.1038/srep35070.

[73] H. Taha, The potential for air-temperature impact from large-scale deployment of solar photovoltaic arrays in urban areas, Sol. Energy. 91 (2013) 358–367. https://doi.org/10.1016/j.solener.2012.09.014.

[74] G.B. Cavadini, L.M. Cook, Green and cool roof choices integrated into rooftop solar energy modelling, Appl. Energy. 296 (2021) 117082. https://doi.org/10.1016/j.apenergy.2021.117082.

[75] A. Scherba, D.J. Sailor, T.N. Rosenstiel, C.C. Wamser, Modeling impacts of roof reflectivity, integrated photovoltaic panels and green roof systems on sensible heat flux into the urban environment, Build. Environ. 46 (2011) 2542–2551. https://doi.org/10.1016/j.buildenv.2011.06.012.

[76] Australian Government Bureau of Meteorology, New South Wales Weather Observations, (2023). http://www.bom.gov.au/nsw/observations/index.shtml?ref=hdr (accessed June 14, 2023).

[77] S. Wilcox, C.A. Gueymard, Spatial and temporal variability of the solar resource in the united states, 39th ASES Natl. Sol. Conf. 2010, Sol. 2010. 2 (2010) 1389–1409.

[78] M.A. Imteaz, A. Ahsan, Solar panels: Real efficiencies, potential productions and payback periods for major Australian cities, Sustain. Energy Technol. Assessments. 25 (2018) 119–125. https://doi.org/10.1016/j.seta.2017.12.007.

[79] D.T. Reindl, W.A. Beckman, J.A. Duffie, Diffuse fraction correlations, Sol. Energy. 45 (1990) 1–7. https://doi.org/https://doi.org/10.1016/0038-092X(90)90060-P.

[80] F. Lindberg, B. Holmer, S. Thorsson, SOLWEIG 1.0 – Modelling spatial variations of 3D radiant fluxes and mean radiant temperature in complex urban settings, Int. J. Biometeorol. 52 (2008) 697–713. https://doi.org/10.1007/s00484-008-0162-7.

[81] Australian Bureau of Statistics, Regional population, 2021-22 financial year, (2023). https://www.abs.gov.au/statistics/people/population/regional-population/latest-release (accessed June 14, 2023).

[82] B. Jacbos, N. Mikhailovich, C. Delaney, Benchmarking Australia's Urban Tree Canopy: An i-Tree Assessment, Final Report 2014, (2014) 47.

[83] Australian Energy Market Operator (AEMO), Electricity Demand Forecasting Methodology Information Paper Important notice PURPOSE, (2019).

[84] G.T. Klise, J.S. Stein, Models used to assess the performance of photovoltaic systems, Sandia Natl. Lab. (2009) 1–67. https://doi.org/10.2172/974415.

[85] S.N. Laboratoraties, pvlib _ python Documentation, (2021).

[86] R.R. Perez, P. Ineichen, E.L. Maxwell, R.D. Seals, A. Zelenka, Dynamic global-to-direct irradiance conversion models, in: ASHRAE Trans., 1992: pp. 354 – 369. https://www.scopus.com/inward/record.uri?eid=2-s2.0-0026995098&partnerID=40&md5=e893277590eb26bb6e80f65f5d7b8e6b.

[87] S. Memme, M. Fossa, Maximum energy yield of PV surfaces in France and Italy from climate based equations for optimum tilt at different azimuth angles, Renew. Energy. 200 (2022) 845–866. https://doi.org/10.1016/j.renene.2022.10.019.

[88] K.A. Klise, J.S. Stein, J. Cunningham, Application of IEC 61724 Standards to Analyze PV System Performance in Different Climates, in: 2017 IEEE 44th Photovolt. Spec. Conf., 2017: pp. 3161–3166. https://doi.org/10.1109/PVSC.2017.8366666.

[89] T. Dierauf, A. Growitz, S. Kurtz, C. Hansen, Weather-Corrected Performance Ratio, NREL Tech. Rep. NREL/TP-5200-57991. (2013) 1–16.

[90] A. Driesse, J.S. Stein, M. Theristis, Improving Common PV Module Temperature Models by Incorporating Radiative Losses to the Sky, (2022).

[91] C. Booten, N. Kruis, C. Christensen, Identifying and Resolving Issues in EnergyPlus and DOE-2 Window Heat Transfer Calculations, (2012).

[92] E. Kaplani, S. Kaplanis, PV Module Temperature Prediction at Any Environmental Conditions and Mounting Configurations, (2020) 921–933. https://doi.org/10.1007/978-3-030-18488-9_77.

[93] D.D. Silva, V. Marson, R.R. de Souza, J.D. de Oliveira, J.B.C. Silva, E.M. Cardoso, A new predictive model for a photovoltaic module's surface temperature, Energy Reports. 8 (2022) 15206–15220. https://doi.org/10.1016/j.egyr.2022.11.094.

[94] A. Karn, V. Chintala, S. Kumar, An investigation into sky temperature estimation, its variation, and significance in heat transfer calculations of solar cookers, Heat Transf. - Asian Res. 48

(2019) 1830–1856. https://doi.org/10.1002/htj.21459.

[95] S. Aigarni, D. Nutter, Survey of sky effective temperature models applicable to building envelope radiant heat transfer, ASHRAE Conf. 121 (2015) 351–363. https://doi.org/10.13140/RG.2.1.4212.5526.

[96] W.C. Swinbank, Long-wave radiation from clear skies, Q. J. R. Meteorol. Soc. 89 (1963) 339–348.

[97] H. Nowak, The sky temperature in net radiant heat loss calculations from low-sloped roofs, Infrared Phys. 29 (1989) 231–232. https://doi.org/10.1016/0020-0891(89)90055-9.